Technical University of Denmark

DTU

Final Report on Investigations of the influence of Helium concentration and implantation rate on Cavity Nucleation and Growth during neutron irradiation of Fe and EUROFER 97

Eldrup, Morten Mostgaard; Singh, Bachu Narain; Golubov, S.

Publication date:
2010

Document Version
Publisher's PDF, also known as Version of record

Link back to DTU Orbit

DTU Library
Technical Information Center of Denmark

DTU

Final Report on Investigations of the Influence of Helium Concentration and Implantation rate on Cavity Nucleation and Growth during Neutron Irradiation of Fe and EUROFER 97

Risø-R-Report

M. Eldrup, B.N. Singh and S.I. Golubov
Risø-R-1619(EN)
September 2010
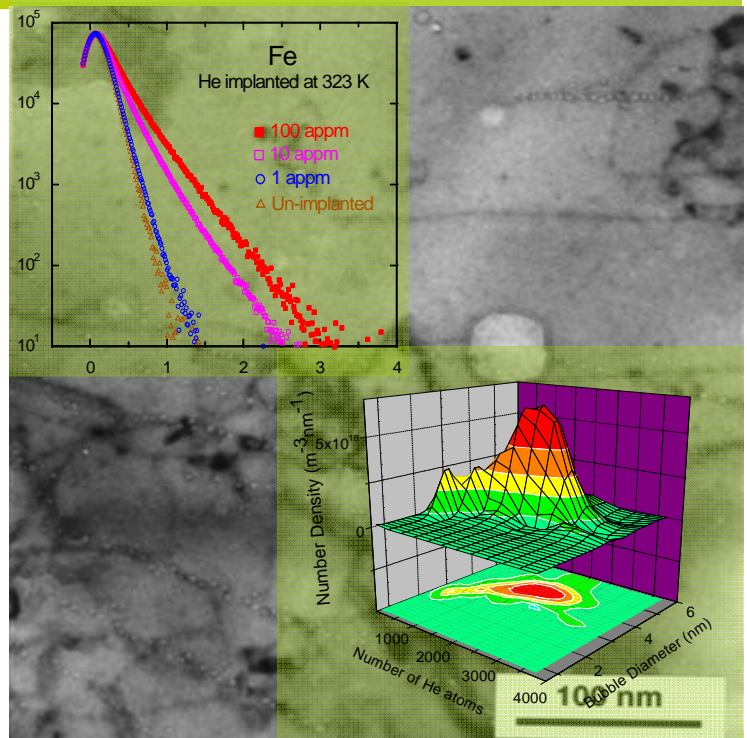
Author: M. Eldrup[1], B.N. Singh[1] and S. Golubov[2]
Title: Final Report on Investigations of the influence of Helium concentration and implantation rate on Cavity Nucleation and Growth during neutron irradiation of Fe and EUROFER 97
Division: Materials Research Division

[1] Materials Research Division, Risø National Laboratory for Sustainable Energy, Technical University of Denmark, DK-4000 Roskilde, Denmark
[2] Materials Science and Technology Division, Oak Ridge National Laboratory, P.O. Box 2008, Oak Ridge, TN 37831-6376, USA

Abstract

This report presents results of investigations of damage accumulation during neutron irradiation of pure iron and EUROFER 97 steel with or without prior helium implantation. The defect microstructure, in particular the cavities, was characterized using Positron Annihilation Spectroscopy (PAS) and Transmission Electron Microscopy (TEM). The PAS investigations revealed a clear difference between the He implantation effects in Fe and EUROFER 97 at 623 K. For both materials the mean positron lifetimes increased with He dose in the range 1 – 100 appm, although the increase was stronger for Fe than for EUROFER 97 and for both materials smaller for implantation at 623 K than at 323 K. This lifetime increase is due primarily to the formation of He bubbles. For He doses of 10 – 100 appm cavity sizes and densities in Fe were estimated to be 1.7 – 2.8 nm and 4 - 14×10^{21} m^{-3}, respectively. Neutron irradiation after He implantation in general leads to an increase of both cavity sizes and densities. Estimates of cavity sizes and densities in EUROFER 97 after neutron irradiation with or without prior helium implantation are rather uncertain, but lead to values of the same order as for iron. TEM cannot resolve any cavities in Fe or EUROFER 97 after implantation of 100 appm He neither at 323 K nor at 623 K. However, neutron irradiation at 623 K to a dose level of 0.23 dpa in Fe is observed to lead to cavities with sizes of about 4 nm and densities of about 1.5×10^{21} m^{-3}. He implantation (100 appm) prior to neutron irradiation results in a cavity density increase to $\sim 1 \times 10^{22}$ m^{-3}. In EUROFER 97 a very inhomogeneous cavity distribution, formed at dislocations and interfaces, is observed after He implantation with subsequent neutron irradiation. In addition, a very low density of very large voids have been observed in Fe (without He) neutron irradiated at 323 K, already at a dose level of 0.036 dpa. Detailed numerical calculations within the framework of the Production Bias Model have been carried out for neutron irradiation with and without prior He implantation and for different implantation rates for comparison with the experimental results. Further, the purpose was to evaluate the role of helium in cavity nucleation and growth during 14 MeV neutron irradiation in a fusion reactor. Calculations were carried out for the experimental temperatures of 323 K and 623 K, i.e. below and above the recovery stage V. In general, the calculations agree qualitatively with the experimental observations and in some cases quantitatively. In this way the calculations give an experimentally supported detailed insight into the evolution of the cavity microstructure under different conditions.

Contents

1. Introduction

Effects of neutron irradiation on defect accumulation and its impacts on physical and mechanical properties of the reduced activation ferritic-martensitic (RAFM) steels are being extensively studied internationally since they are considered to be candidate materials for the blanket and the first wall of fusion reactors (e.g. DEMO and Commercial) [1]. These alloys are considered to have a number of more attractive properties than alternative structural materials such as austenitic stainless steels or vanadium alloys [2].

Although the ferritic-martensitic class of steels are resistant to void swelling and maintain good fracture toughness at irradiation temperatures above 673 K [3], they are prone to loss of ductility at lower irradiation temperatures [4, 5]. Furthermore, we have demonstrated recently that in pure iron as well as F82H steel irradiation with fission neutrons causes void formation already at temperatures as low as 323 - 373 K [6-8]. This is in agreement with general experimental observations that voids in bcc metals and alloys are formed at relatively low temperatures, i.e. close to the recovery stage III (see [9] for a review). It is interesting to note that even though a high density of voids are nucleated in bcc metals and alloys, the swelling rate remains very low because of very low growth rate of the densely populated cavities. This has been rationalized in terms of production of highly glissile clusters of self-interstitial atoms (SIAs) directly in the cascades and subcascades produced by fission neutrons [10]. It should be recognized here that these results and conclusions are valid only for irradiation in the environment of fission neutrons where the production rate of helium is very low. The fact that these alloys are expected to be exposed to 14 MeV neutrons in a fusion reactor (e.g. DEMO) introduces a complication due to concurrent generation of helium atoms at a relatively high He-to-displacement ratio (~10-20 appm/dpa) and at damage rates of $\sim 10^{-6}$ dpa/s in the form of cascades and subcascades. This is a matter of serious concern from the point of view of the application of these alloys in the structural components of DEMO. Unfortunately, very little is known at present about the effects of helium atoms in the environment of a fusion reactor on cavity nucleation and growth (i.e. swelling).

Over the years many attempts, both theoretical and experimental, have been made to understand the phenomenon of helium assisted cavity nucleation and growth in metals and alloys. Because of the lack of appropriate sources of 14 MeV neutrons, however, most of the experimental investigations of this phenomenon have been carried out using the technique of helium implantation and post-implantation irradiation with light and/or heavy ions. In a few cases the helium implanted specimens have been irradiated with fission neutrons prior to post-irradiation examinations. Experimental results of a variety of such experiments have been compiled and analysed in terms of the existing theoretical models [11]. In [11] the influence of displacement damage on helium diffusion and bubble nucleation is also briefly described.

The effects of helium generation rate on cavity nucleation and growth behaviour in high purity aluminium have been discussed in [12].

In spite of the detailed analysis of the experimental results and relevant theoretical considerations presented in [11], it was not possible to draw a firm conclusion regarding the mechanisms of helium diffusion and bubble nucleation and growth particularly in the low temperature regime (i.e. below about 0.5 T_m where T_m is the melting temperature in Kelvin).

It is worth noting that there is a serious lack of experimental results in this temperature regime even though this regime is the most relevant regime from the point of view of technological application. One of the reasons for the lack of such results may be the difficulty in obtaining data on bubble size and density after helium implantation in the low temperature regime. The difficulty arises because during helium implantation in this low temperature regime, particularly at relatively high implantation rates, high densities of rather small bubbles are likely to be formed and these bubble are likely to be too small to be characterized quantitatively using the technique of transmission electron microscopy (TEM). The lack of such data, on the other hand, makes it practically impossible to identify the mechanisms and kinetics of helium diffusion and bubble nucleation and to be able to distinguish them from the mechanism and kinetics of post-nucleation growth. In the past, this has been the major problem in the analysis of the results obtained using the implantation technique.

In recent years, we and others have demonstrated that positron annihilation spectroscopy (PAS) can be successfully used to identify vacancy clusters in the size range from single vacancies to large three-dimensional cavities. This means that using PAS technique cavities can be identified already in their embryonic state. The post-nucleation coalescence and growth of these cavities can be followed using the PAS and the TEM techniques.

The main objective of the present work was first to obtain such experimental results characterising the cavity evolution already during the implantation stage and then to follow the evolution of these cavities after post-implantation neutron irradiation to different displacement doses. The second objective of the present work was to perform theoretical analysis of these results to help understand the role of helium atoms in controlling the kinetics of cavity nucleation and growth during implantation and transformation of the cavity population produced during implantation when exposed to neutron irradiation. Furthermore, an analysis of these experimental and theoretical results should allow us to assess the effect of concurrent productions of helium atoms and displacement cascades on cavity nucleation and growth in materials exposed to 14 MeV neutrons in a fusion reactor.

In a previous work [13] we have already reported experimental and theoretical results obtained on physical and mechanical properties of iron and steel that had been helium implanted and neutron irradiated at a temperature of about 323 K. In the present report results are described which have been obtained for helium implantation and neutron irradiation of iron and

EUROFER 97 carried out at a temperature of 623 K. Also included in the present report are some additional results obtained at 323 K. The next chapter describes the materials which have been investigated, the implantation and irradiation characteristics as well as some experimental details of the PAS experiments and TEM studies. Chapter 3 presents the PAS results in terms of positron lifetime parameters and Doppler broadening S- and W-parameters as well as cavity sizes and densities derived from PAS and TEM. Chapter 4 gives a detailed account of the results of the theoretical treatment of the cavity evolution under conditions similar to the ones used in the experimental work. Finally, Chapter 5 summarizes and presents conclusions that may be drawn from the present work.

2. Materials and Experimental Procedure

Specimens of pure (99.99 wt%) iron and EUROFER 97 were investigated in the present work. The pure iron specimens were fabricated from thin (0.25 mm) sheets. They were cold rolled in steps of 25% reduction with intermediate anneals (0.5 hours, 923 K, vacuum-quench), cut to shape (strips of $20 \times 3 \times 0.1$ mm^3) and finally heat treated 2 hours at 923 K and vacuum-quenched. The specimens of EUROFER 97 reduced activation steel was fabricated from the common European stock available at PSI (Switzerland). They were rolled in steps of 25% reduction with intermediate anneals (1 hour, 1023 K, vacuum-quench), cut to shape (strips of $20 \times 3 \times 0.1$ mm^3) and finally heat treated 0.5 hours at 1253 K and vacuum-quenched followed by 1.5 hours, 1023 K, furnace cooling [14]. Every specimen was identified by a number engraved at one end of the strip before implantation and irradiation. Some specimens of pure iron (i.e. without helium) were irradiated in the as-annealed condition. Similarly, some specimens of EUROFER 97 steel were irradiated in the as-tempered condition. Irradiations were carried out in the BR-2 reactor at Mol.

Strip specimens of both pure iron and EUROFER 97 steel were implanted with helium at Forschungszentrum Jülich (Germany). A beam of 28 MeV α-particles, energy degraded by a rotating wheel equipped with Al foils, was used for implantation of the specimens to provide a homogeneous He concentration throughout a depth of about 100 μm (i.e. the specimen thickness) over an area of about 13×12 mm^2 (covering the mid-part of three strip specimens placed side by side). The implantations were carried out at 623 K to concentration levels of 1, 10 and 100 appm of helium at implantation rates in the range of 1.2×10^{-3} to 1.2×10^{-2} appm He/s [14] (Table 1). On average, each implanted He atom gives rise to 154 atomic displacements. Hence, the implantation gives rise to displacement damage doses of 1.5×10^{-4}, 1.5×10^{-3} and 1.5×10^{-2} dpa, respectively for the three concentrations of implanted helium (Table 1), with displacement damage rates in the range of 1.85×10^{-7} to 1.85×10^{-6} dpa/s. Both un-implanted and He-implanted specimens were irradiated with fission neutrons in the BR-2 reactor at Mol (Belgium) at 623 K with a displacement dose rate of ~4.5×10^{-8} dpa/s to doses of 0.08, 0.15 and 0.23 dpa. Unfortunately, several specimens got

deformed to varying degrees during the specimen handling, leaving the microstructure of some of them ill-defined. Similarly, identification numbers on several of the specimens turned out to be damaged after the neutron irrradiation to such a degree that the specimens could not be identified. These specimens were therefore not further investigated.

For each PAS measurement two samples of approximately 5×3 mm^2 were cut from one strip specimen. The samples were cleaned by electropolishing prior to the measurements. A conventional positron lifetime spectrometer was used. For some of the He implanted specimens, measurements were carried out with both the beam entry side and the "back" side of the samples facing the positron source.

For transmission electron microscopy (TEM) investigations, ~1 mm wide and ~0.1 mm thick specimens were prepared from the implanted, the irradiated and from the implanted and irradiated strips. Thin foils were obtained from these strips by electro-polishing at 18V in a solution of 10% perchloric acid in ethanol at 253 K. The thin foils were examined in the 200 kV JEOL 2000 FX electron microscope at Risø DTU or in the 200 kV Philips CM 20 electron microscope at the Niels Bohr Institute, University of Copenhagen.

3. Results

3.1 Positron Annihilation Spectroscopy

Positron annihilation spectroscopy (PAS) has in recent years been accepted as a useful method for defect spectroscopy, in particular in studies of metals and semiconductors. The physical basis for this is the fact that positrons injected into a material may get trapped at defects where the atomic and electronic densities are lower than the average density in the bulk, i.e vacancies, vacancy clusters (including voids and bubbles) and dislocations. Since positrons and electrons are antiparticles, an injected positron will annihilate with an electron of the material. As a result, γ-rays will be emitted, that carry information about the state of the positron before annihilation, and by proper measurement of the emitted γ-quanta it is possible to obtain useful information about the defects that trap the positrons. This is in brief the physics behind PAS. A more detailed discussion and relevant references can be found in e.g. [15, 16].

In the present work mainly the positron annihilation lifetime spectroscopy (PALS) has been used to measure the distributions of lifetimes of injected positrons, so-called positron lifetime spectra. Normally, regions of lower-than-average atomic density in crystals also have lower-than-average electron density. The lifetime of positrons trapped in defects depends on the average electron density in the defects (the lower the electron density, the longer is the lifetime). So in principle, each type of defect gives rise to a characteristic positron lifetime, τ_i. In cases where several types of defects are present in a

sample, a measured lifetime spectrum will therefore consist of several lifetime components. Each component is a decaying exponential, the slope of which equals the annihilation rate (= τ_i^{-1}). Hence, a spectrum (distribution of lifetimes) can be described by

$$N(t) = \sum_i A_i \exp\left(-t / \tau_i\right), \qquad (1)$$

where t is the time. The so-called intensity I_i of the i'th component is the area of this component, normally given in percent of the total area under the spectrum by

$$I_i = \frac{A_i \tau_i}{\sum_i A_i \tau_i} 100\%. \qquad (2)$$

Many examples of measured positron lifetime spectra are shown in figures 1 – 3 and 5 - 7. The figures display both single- and multi-component spectra. Due to a finite time resolution of the lifetime spectrometer, the peaks of the spectra are rounded.

A parameter which is often used to characterize a lifetime spectrum in a simple, quantitative way is the *mean lifetime*

$$\tau_{mean} = \frac{\int tN(t)dt}{\int N(t)dt} = \sum_i I_i \tau_i. \qquad (3)$$

Qualitatively, the mean lifetime represents the inverse of the average slope of a lifetime spectrum (i.e. a steep slope is equivalent to a small lifetime).

In bulk Fe the positron lifetime is 106 ps, while in defects such as mono-vacancies, dislocation lines and loops the lifetimes are found to be in the range of ~120 - ~180 ps. The lifetime of positrons trapped in three-dimensional vacancy agglomerates (cavities, voids) increases with the size of the cavities, the lifetime value thus being a measure of the cavity size, up to a saturation value of about 500 ps for voids containing more than ~ 40 - 50 vacancies. The presence of He (or other gases) in a cavity reduces the positron lifetime compared to the lifetime value in an empty cavity of the same size [17]. Theoretical, quantitative estimates of the lifetime dependence on cavity size as well as density of helium (and other inert gases) have been made for several metals [17 - 19].

In the following we shall describe PALS results obtained for iron and EUROFER 97 implanted at ~ 623 K with He to different concentration levels, with different implantation rates and - for some specimens - subsequently irradiated with neutrons to different dose levels, also at 623 K. In order to illustrate directly the obtained positron lifetime data for implanted and irradiated iron and EUROFER 97 steel, we present some of the measured lifetime spectra. For easy comparison, we also include some data on specimens implanted with He and neutron irradiated at 323 K [13]. Since ref. [13] was published more measurements have been carried out on specimens that were He implanted and/or neutron irradiated at 323 K. The results from these measurements have been included in the present report. Therefore, at some places the data presented here are more well-defined than those in [13] and may therefore deviate somewhat from those.

In addition to PALS measurements of as-implanted and/or as-irradiated specimens mentioned above an investigation of the annealing behaviour of Fe implanted at 323 K with 100 appm He was carried out (collaboration with T. Toyama, Z. Tang, Y. Nagai and M. Hasegawa of the Institute for Materials Research, Tohoku University, Japan). Both PALS as well as another positron annihilation spectroscopy, namely Coincidence Doppler Broadening (CDB) were used for this study. CDB measures the momentum distribution of the electrons with which the positrons annihilate and therefore may provide some information about the chemical identity of the atoms that surround the positrons.

Table 1. Positron lifetimes and intensities for Fe that has been He implanted and neutron irradiated at 623 K. The data shown are a selection of typical results for the specimens that have been measured. The lifetimes τ_3 are due to 3-dimensional cavities that consist of 10 vacancies or more, while the lifetimes τ_2 are due to other defects, including vacancy "clusters" with ~ 1 - 5 vacancies. The mean lifetimes in the last column are the ones plotted in Fig. 4.

He Concentration (appm)	He Displacement Dose (dpa)	He Implantation Rate (appm /s)	Neutron Dose (dpa)	τ_1 (ps)	τ_2 (ps)	τ_3 (ps)		I_1 (%)	I_2 (%)	I_3 (%)		Mean lifetime (ps)
1	0.00015	0.012	0	100 ± 1	210 ± 6			93.6 ± 0.6	6.4 ± 0.6			107
1	0.00015	0.0036	0	103 ± 1	262 ± 10			97.5 ± 0.3	2.6 ± 0.3			107
1	0.00015	0.0012	0	97 ± 1	164 ± 4			84.9 ± 1.8	15.1 ± 1.8			107
10	0.0015	0.012	0	99 ± 1	255 ± 4			85.7 ± 0.6	14.3 ± 0.6			121
10	0.0015	0.012	0	96 ± 1	268 ± 1			88.4 ± 0.2	11.6 ± 0.2			116
10	0.0015	0.012	0	103 ± 1	254 ± 4			80.8 ± 0.8	19.2 ± 0.8			132
10	0.0015	0.012	0	90 ± 1	196 ± 2			74.1 ± 0.7	26.0 ± 0.7			117
10	0.0015	0.0036	0	89 ± 1	184 ± 6	474 ± 80		75.2 ± 1.9	24.3 ± 1.7	0.5 ± 0.3		114
10	0.0015	0.0012	0	64 ± 2	165 ± 2	385 ± 26		36.0 ± 1.0	62.7 ± 0.7	1.3 ± 0.3		131
100	0.015	0.012	0	25 ± 5	115 ± 12	294 ± 3		28.0 ± 1.7	19.5 ± 1.2	52.5 ± 1.1		184
100	0.015	0.012	0	60 ± 1	278 ± 4	465 ± 41		44.6 ± 0.3	52.2 ± 1.2	3.2 ± 1.4		187
100	0.015	0.012	0	69 ± 2	255 ± 6	510 ± 63		41.3 ± 0.9	55.1 ± 1.1	3.6 ± 1.6		187
100	0.015	0.012	0	48 ± 4	154 ± 8	262 ± 1		26.4 ± 1.9	46.8 ± 2.4	26.9 ± 3.8		155
100	0.015	0.0036	0	68 ± 1	200 ± 4	334 ± 10		42.0 ± 0.7	48.5 ± 1.0	9.5 ± 1.5		158
100	0.015	0.0012	0	71 ± 1	193 ± 3	352 ± 10		36.3 ± 0.9	56.5 ± 0.5	7.3 ± 1.0		160
0	0	0	0.23	79 ± 2	203 ± 5	519 ± 8		51.2 ± 1.5	38.1 ± 1.1	10.7 ± 0.5		173
10	0.0015	0.012	0.15	61 ± 2	178 ± 6	388 ± 5		36.2 ± 1.3	37.7 ± 0.7	26.0 ± 1.1		193
10	0.0015	0.012	0.23	45 ± 4	167 ± 5	379 ± 7		26.8 ± 1.4	50.3 ± 0.8	22.8 ± 1.3		182
100	0.015	0.012	0.15	54 ± 3	191 ± 4	410 ± 4		20.7 ± 0.7	51.9 ± 0.5	27.4 ± 0.8		222
100	0.015	0.012	0.23	59 ± 5	186 ± 6	392 ± 6		20.5 ± 1.5	54.2 ± 0.9	25.3 ± 1.5		212

3.1.1 Iron

Figure 1 shows a comparison of positron lifetime spectra for Fe implanted with 100 appm of helium at 323 K and 623 K, respectively. The larger effect of implantation at 323 K than at 623 K is associated with the generation of a high density of small cavities at the lower temperature, but an appreciably lower density of larger He bubbles at the higher temperature.

Figure 2 clearly shows that in Fe, the positron lifetime increases with increasing concentration of implanted He at both 323 K and 623 K due to the increasing displacement dose created by the He (note that implantation with 1, 10 and 100 appm He leads to displacement doses of 1.5×10^{-4}, 1.5×10^{-3}, and 1.5×10^{-2} dpa, respectively; see Table 1).

In Figure 3 the effect of neutron irradiation after He implantation is shown, again at both 323 K and 623 K. For comparison also the spectra for He implantation (100 appm) without neutron irradiation as well as the spectra for only neutron irradiation (0.01 dpa at 323 K and 0.23 dpa at 623 K) are shown. At the lower temperature the spectra are rather similar, the one for only He implantation though falls mainly below the other two spectra. In addition, comparing the spectra for neutron irradiated samples, a small effect can be seen of He implantation prior to neutron irradiation. At 623 K on the other hand, there is a clear effect of He implantation prior to neutron irradiation.

In order to give an overview of all the data obtained for iron which has either been implanted with helium, neutron irradiated or neutron irradiated after helium implantation, Figure 4 shows mean positron lifetimes as functions of total displacement dose at both 323 K and 623 K. The mean lifetimes (Eq. 3) were derived from the spectra shown in Figures 1 - 3 as well as from spectra for other specimens. For He implantation at both temperatures the mean lifetime increases with He concentration and hence displacement dose (as mentioned above, implantation of 100 appm helium gives rise to a displacement dose of 0.015 dpa). Qualitatively, a mean-lifetime increase can be ascribed to an increase in density of defects and/or size of cavities. The difference in mean lifetime after implantation to the same He concentration at the two temperatures is mainly due to a much larger cavity density at 323 K than at 623 K (see below). Figure 4 also demonstrates that the influence of He implantation prior to neutron irradiation is quite different at the two temperatures. At 323 K the presence of He has only a moderate influence on the result of neutron irradiation, while at 623 K the presence of He has a clear effect on the cavity nucleation during neutron irradiation.

The brief mean-positron-lifetime description in the above paragraph for some of the measured Fe specimens is meant to give a simple qualitative impression of the general trend of the results. Also a more detailed analysis of the measured lifetime spectra was carried out: All spectra for implanted and/or irradiated specimens were composed of more than one lifetime component (see Figures 1 - 3) and could be decomposed into two or three

lifetime components using the PALS*fit* program [20]. Some typical results are shown in Table 1.

When comparing the lifetimes (τ_i) and intensities (I_i) in each column in Table 1 for 1, 10 and 100 appm He, respectively, it is obvious that each of these parameters show an appreciable scatter, even for specimens with the same He implantation rates. As a consequence of the scatter it is not possible to define any trend in the data that can be correlated with the He implantation rate. Normally, the mean lifetime that can be derived from a measured lifetime spectrum is more well-defined than the lifetimes and intensities of the various components into which the spectrum can be decomposed. However, also the mean lifetimes in Table 1 clearly scatter, even for nominally identical specimens. Thus, attempts to correlate mean lifetimes with implantation rates were unsuccessful. On the other hand the mean lifetimes clearly correlate with total He concentration (Figures 2 and 4, Table 1).

3.1.2 EUROFER 97

Figure 5 shows a comparison of positron lifetime spectra for EUROFER 97 implanted with 100 appm of helium at 323 K and 623 K, respectively, as well as the spectrum for un-implanted (i.e. as-tempered) EUROFER 97. Like for iron, the effect of implantation at 323 K is larger than at 623 K, although not as pronounced as observed for iron. The difference between implantation at 323 K and at 623 K is associated with the generation of a high density of small cavities at the lower temperature, but a lower density of larger He bubbles at the higher temperature.

The lifetime spectrum for un-implanted specimens shows a somewhat longer average lifetime than for pure Fe (compare with Fig. 1, 2 or 3). The quantitative analysis (Table 2) shows that a major fraction of the positrons have a lifetime of 145 ps, which means that they are trapped in a population of defects, present already before He implantation and neutron irradiation. This lifetime is close to the one found for as-tempered F82H steel [21] and it is reasonable to ascribe the lifetime to positrons trapped at dislocations. This defect population, maybe somewhat modified, is likely to be present also in the implanted and irradiated specimens and will make a quantitative analysis of the results for such specimens more uncertain than is the case for pure Fe.

Figure 6 shows positron lifetime spectra for EUROFER 97, which was implanted with 1, 10, and 100 appm of He at 323 K (upper frame) and at 623 K (lower frame). Figure 6 clearly shows that in EUROFER 97 like in iron, the positron lifetime increases with increasing concentration of implanted He at both temperatures. Like for iron this rise is associated with the increasing displacement dose created by the He (implantation with 1, 10 and 100 appm He leads to displacement doses of 1.5×10^{-4}, 1.5×10^{-3}, and 1.5×10^{-2} dpa, respectively).

In Figure 7 the effect of neutron irradiation after He implantation is shown, again at both 323 K and 623 K. For comparison also the spectra for He implantation (100 appm) without neutron irradiation as well as the spectra for

only neutron irradiation (0.01 dpa at 323 K and 0.1 dpa at 623 K) are shown. At the lower temperature the spectra are rather similar, although the one for only neutron irradiation falls slightly above the other two spectra. Thus, at 323 K the displacement dose seems to be the dominant factor (implantation of 100 appm helium gives rise to a displacement dose of 0.015 dpa), while the presence of He has only a minor effect. On the other hand, at 623 K only a small effect of displacement damage is observed unless He is present.

Figure 8, which shows the mean positron lifetime as a function of total displacement dose, summarizes the data presented in Figs. 5 - 7 as well as data from spectra for other specimens. The relatively small effect of neutron irradiation with or without prior He implantation is clearly displayed. As Fig. 8 shows, in the investigated He concentration range of 0 – 100 appm He changes of the mean lifetime fall in the range up to 30 ps for EUROFER 97 at 623 K, while for Fe the range of mean lifetime variations is about 60 ps at the same temperature (Fig. 4). At 323 K the changes of the mean lifetime are appreciably larger (about 95 ps and 135 ps, respectively).

Like for Fe, detailed quantitative analyses of the positron lifetime spectra were carried out for EUROFER 97. The results are shown in Table 2. As shown in the table, all lifetime spectra could be resolved into two or three components. Like for iron (Table 1) there is an appreciable scatter of the data (including the mean lifetime) for nominally identical specimens, and it is not possible to identify any rate effect of He implantation. On the other hand, like for Fe, one can see a clear dependence of the mean lifetime on He concentration (Figs. 6 and 8).

3.1.3 Annealing of He implanted Iron: PALS and CDB results

In order to investigate the question of the character of the cavities which are created in iron during He implantation at a temperature of 323 K, an isochronal annealing experiment in the temperature range from 323 K to 1173 K has been carried out on Fe implanted at 323 K with 100 appm He. Both positron lifetime as well as Coincidence Doppler Broadening (CDB) measurements were carried out in a collaboration with T. Toyama, Z. Tang, Y. Nagai and M. Hasegawa of the Institute for Materials Research, Tohoku University, Japan. Figure 9 shows the results of the positron lifetime measurements. Three lifetime components could be resolved in the temperature range from 323 K to 973 K. The two longer lifetimes (τ_2 and τ_3) and their intensities (I_2 and I_3) show the presence of vacancy sized defects (τ_2) and 3-dimensional vacancy agglomerates (τ_3). The magnitude of the long lifetime τ_3 (~360 ps) is equivalent to empty cavities containing on average ~ 10 - 15 vacancies [22] or He bubbles of bigger sizes. There is a distinct decrease of this lifetime at annealing temperatures in the range of 573 - 623 K. This shows that in this temperature range either the average cavity size decreases or the average density of helium in the cavities increases, or both. Above 623 K τ_3 hardly changes with annealing temperature until 873 K. At

and above 873 K τ_3 increases again, which is indicative of a coarsening of the cavity population.

Table 2. Positron lifetimes and intensities for EUROFER 97 that was He implanted and neutron irradiated at 623 K. The data in the table are a selection of typical results for the specimens that have been measured. The lifetimes τ_3 are due to small 3-dimensional cavities of less than about 10 vacancies, while the lifetimes τ_2 are due to other defects, including defects already present in the un-irradiated specimens as well as small vacancy "clusters" consisting of a few vacancies. The mean lifetimes in the last column are the ones plotted in Fig. 8.

He Concentration (appm)	He Displacement Dose (dpa)	He Implantation Rate (appm/s)	Neutron Dose (dpa)	τ_1 (ps)	τ_2 (ps)	τ_3 (ps)		I_1 (%)	I_2 (%)	I_3 (%)		Mean lifetime (ps)
0	0	0	0	63 ± 11	145 ± 3			14.1 ± 3.4	85.9 ± 3.4			133
1	0.00015	0.0036	0	57 ± 3	153 ± 2	313 ± 67		21.7 ± 1.2	77.5 ± 0.7	0.8 ± 0.7		133
10	0.0015	0.012	0	79 ± 3	185 ± 1			28.9 ± 1.3	71.1 ± 1.3			154
10	0.0015	0.012	0	45 ± 3	124 ± 3	212 ± 2		15.8 ± 1.1	51.9 ± 1.0	32.4 ± 1.9		140
10	0.0015	0.0036	0	71 ± 3	176 ± 5	308 ± 37		30.0 ± 2.0	66.6 ± 1.0	3.4 ± 2.2		149
100	0.015	0.012	0	55 ± 3	157 ± 4	308 ± 4		26.5 ± 1.6	50.4 ± 0.8	23.1 ± 1.4		165
100	0.015	0.012	0	52 ± 6	143 ± 5	279 ± 8		19.8 ± 3.0	55.9 ± 1.1	24.5 ± 2.5		158
100	0.015	0.0036	0	71 ± 2	189 ± 4	334 ± 9		29.3 ± 1.2	59.4 ± 0.8	11.3 ± 1.6		171
0	0	0	0.08	77 ± 4	165 ± 4			33.1 ± 3.2	66.7 ± 2.9			136
0	0	0	0.23	72 ± 6	168 ± 7	330 ± 85		27.4 ± 3.8	71.3 ± 1.9	2.3 ± 2.6		147
100	0.015	0.012	0.08	57 ± 10	156 ± 7	333		20.4 ± 4.0	52.5 ± 5.0	27.1 ± 1.2		184
100	0.015	0.012	0.23	51 ± 9	163 ± 7	375 ± 12		20.0 ± 2.6	60.5 ± 1.4	19.5 ± 2.0		182

Fig. 10 shows the results of the CDB measurements, recorded simultaneously with the lifetime data in Fig. 9. CDB measures essentially the momentum distribution of those electrons with which the positrons annihilate. A measured momentum distribution may be considered as a superposition of the distribution for the bulk material and the distribution for the defects which trap the positrons, i.e.

$$F_{meas} = (1 - \alpha)F_{bulk} + \alpha F_{defect}. \tag{4}$$

The bell like shape of CDB curves is often characterized in a simple way by two parameters, S and W. S represents the area of the central part of the distribution (due mainly to conduction electrons with low momentum) while W measures the area of the wings of the distribution (due mainly to – high momentum - core electrons of the atoms). Hence,

$$S_{meas} = (1 - \alpha)S_{bulk} + \alpha S_{defect}$$
$$W_{meas} = (1 - \alpha)W_{bulk} + \alpha W_{defect}, \tag{5}$$

where $0 < \alpha < 1$ and α increases with increasing defect density.

A useful way of plotting data is to show W_{meas} as a function of S_{meas} in a so-called S-W plot, like the one in Fig. 10. If a series of samples contain the same type of defects, but with different defect densities (and hence different values of α), positron trapping into these defects will result in sets of S- and W-parameters that lie on a straight line in an S-W plot. This is exemplified in Fig. 10 by the green points (and line) for nano-voids of different densities, produced by neutron irradiation. Normally, $S_{defect} > S_{bulk}$ and $W_{defect} < W_{bulk}$ because positrons in cavities preferentially annihilate with conduction electrons rather than core electrons. Hence, with increasing nano-void density the points will move from the upper left-hand corner to the lower right-hand corner as seen in Fig. 10. Deviations from a straight line in an S-W plot indicate that the positrons detect the presence of other chemical species than (in this case) pure iron.

The blue points in Fig. 10 were obtained during the annealing process of Fe implanted with 100 appm of He at 323 K, with some of the annealing temperatures indicated. The behaviour of the blue annealing curve suggests that up to a temperature of ~ 473 K, the detected defects are similar to nano-voids (since the points are close to the green line), while at higher temperatures defects of a different kind are detected. Tang (unpublished) has carried out theoretical calculations of electron momentum distributions in He-containing cavities, as detected by positrons. The calculations show that an increasing density of He in the cavity results in a negative shift of both S and W which is in a qualitative agreement with the observations for annealing above ~ 473 K (Fig. 10). Thus the data in Fig. 10 are consistent with the contention that at low annealing temperatures positrons are mainly detecting cavities with a low He-to-vacancy ratio, while at higher annealing temperatures mainly cavities with a high He-to-vacancy ratio act as trapping centres for positrons.

3.2 Microstructure determined by PAS and TEM

3.2.1 Iron

In spite of the scatter in the PAS data for Fe mentioned above (section 3.1.1) it is possible to make quantitative estimates of the sizes and densities of the cavities in the 10 and 100 appm He-implanted specimens based on averages of the data in Table 1. The cavities give rise to the τ_3 lifetime component with the intensity I_3 (or τ_2, I_2 when only two components can be resolved). Based on the assumption that essentially all implanted He atoms have been trapped in the cavities (He bubbles, with a distribution of sizes and He densities), Jensen et al. [23] developed a methodology by which average sizes and densities of the cavities can be estimated from the positron annihilation lifetime results. Following Jensen's method, we estimated the sizes and densities of He bubbles based on the data in Table 1. The results are shown in Table 3. The estimates for implantation of 10 and 100 appm He reveal that the density of bubbles increases about ten times compared to that of neutron irradiation. In the case of neutron irradiation after implantation of 10 appm He the bubble density slightly increases to the value which is at the same level as it is after implantation of 100 appm. Surprisingly the estimated density for the case of neutron irradiation after implantation of 100 appm He is found to be an order of magnitude smaller than in the case of 10 appm He implantation. The origin of this unexpected result is not clear.

Table 3. Estimates of cavity sizes and densities for Fe implanted with He with or without subsequent neutron irradiation (both at 623 K). The estimates are based on the PAS data in Table 1, using the method by Jensen et al. [22]. In addition, data for neutron irradiation without He implantation are given (the cavity size cannot be derived from PAS in this case, but is taken from TEM and used to determine the cavity density from the PAS results).

He concentration (appm)	Neutron dose (dpa)	Average cavity diameter (nm)	Cavity density (m^{-3})
0	0.23	~4 from TEM (Table 4)	~1×10^{21}
10	0	1.7 ± 0.3	$4 \pm 2\times10^{21}$
100	0	2.8 ± 0.8	$1.4 \pm 0.8 \times10^{22}$
10	Average of data for 0.15 and 0.23	2.0 ± 0.1	$9 \pm 2\times10^{21}$
100	Average of data for 0.15 and 0.23	8.9 ± 0.5	$1.5 \pm 0.2\times10^{21}$

Transmission electron microscopy was carried out on pure Fe specimens that had been neutron irradiated at 623 K with and without pre-implanted helium. Figure 11 shows the cavity structure after neutron doses of 0.08 dpa and 0.23 dpa. The micrographs show the presence of a high density of cavities with

average sizes of a few nano-metres (Table 4). No cavities were observed by TEM in Fe implanted with 100 appm He at 623 K. However, a high density of cavities was observed in the case of neutron irradiation to a dose of 0.23 dpa after implantation of 100 appm He (see Fig. 12). The presence of He during neutron irradiation results in an almost ten times increase in the cavity density, while the average size remains almost unchanged (Table 4).

An additional interesting observation [24] has been that in iron specimens which were neutron irradiation at 323 K to a dose of 0.036 dpa a population of relatively large voids (~90 nm in diameter) of a low density (~1×10^{19} m^{-3}) were present (Fig. 13a). Furthermore, also in iron implanted with 100 appm of helium at 323 K and subsequently neutron irradiated at 333 K to a dose level of 0.1 dpa large cavities (~52 nm in diameter) of a low density (~2×10^{19} m^{-3}) were observed (Fig. 13b) [13].

Table 4. TEM estimates of cavity sizes and densities for Fe neutron irradiated at 623 K with or without prior He implantation (also at 623 K). The estimates are based on a number of micrographs like the ones shown in Figs. 11 and 12.

He concentration (appm)	Neutron dose (dpa)	Average cavity diameter (nm)	Cavity density (m^{-3})
0	0.08	~2.5	~1.5×10^{21}
0	0.23	~4.0	~1.5×10^{21}
100	0	---	---
100	0.23	~3.5	~1×10^{22}

3.2.2 EUROFER 97

As indicated above (Section 3.1.2) and observed by TEM (see below), the microstructure in EUROFER 97 is more complicated than that in pure Fe and the bubbles are distributed heterogeneously, mainly along dislocations. Since quantitative estimates of cavity sizes and densities from PAS data assumes homogeneous distributions of cavities, the heterogeneous distribution in EUROFER 97 makes it more difficult to derive reliable cavity parameters, not least for specimens implanted with low concentrations of He. However, rough estimates of cavity sizes and densities for specimens implanted with 100 appm He, with and without neutron irradiation have been made and are shown in Table 5.

TEM investigations were also carried out on neutron irradiated EUROFER 97 specimens containing 100 appm of helium implanted at 623 K. The specimens were examined in the as-implanted as well as in the post-implantation neutron irradiated conditions. Neutron irradiation was carried out at a temperature of 623 K to a dose level of 0.23 dpa. It is important to note that no cavities were observed in the as-implanted specimens. Even after

Table 5. Rough estimates of cavity sizes and densities for EUROFER-97 implanted with He and neutron irradiated at 623 K. The estimates are based on the PAS data in Table 2, using the method by Jensen et al. [22].

He concentration (appm)	Neutron dose (dpa)	Average cavity diameter (nm)	Cavity density (m^{-3})
100	0	~5	~2×10^{21}
100	0.08	~5	~3×10^{21}
100	0.23	~8	~1×10^{21}

post-implantation neutron irradiation at 623 K, cavities were observed only on the heterogeneously distributed grown-in dislocations (Fig. 14), in contrast to the homogeneous distribution of cavities in Fe (Figs. 11, 12). In other words, cavities in the matrix are too small to become visible in the electron microscope. Thus, the TEM investigations could not be used for a quantitative characterisation of cavity density and size in EUROFER 97, neither in the as-implanted nor post-implantation neutron irradiated conditions. It is worth pointing out here that also in EUROFER 97 relatively large voids of low density are formed during post-implantation neutron irradiation at 623 K (Fig. 14). As mentioned in Section 3.2.1 such large voids have been observed also in the neutron irradiated pure iron with and without implanted helium at the relatively low irradiation temperature of ~ 323 K.

4. Modeling

A realistic modeling of helium-vacancy cluster evolution may provide a better understanding of the role of He in damage accumulation in irradiated materials. Experimental data presented in this report provide unique information for modeling of impact of helium on cavity evolution. Indeed, the irradiations were carried out at two critical temperatures: a) slightly above the recovery stage III which allows a study of cavity evolution at the onset of vacancy mobility, and b) above stage V, that provides an opportunity to study cavity evolution when small vacancy clusters, which are important for the cavity nucleation, become unstable against thermal evaporation. Another important point is related to a combination of different irradiation conditions used here: pure neutron irradiation, He implantation and neutron irradiation after the He implantation at the same temperatures. Such a combination provides an opportunity for a cross check of the numerous parameters that have to be chosen for modeling which is extremely important taking into account that there is large uncertainty in many of them. In addition the irradiations are restricted to relatively small doses (<1 dpa) which is also important for two reasons: a) the mechanisms responsible for damage accumulation operating under cascade damage conditions, which is the case for both neutron irradiation and He implantation regimes, are relatively well understood and described by the "Production Bias Model" (PBM) and b) the calculations can be made with a maximum accuracy in a reasonable

computing time. The calculations presented in the next section attempts to utilize all the advantages mentioned above.

4.1 Background

The literature contains several partial treatments of the problem, i.e. impact of He atoms on cavity evolution, however an accurate solution of the problem is complicated and the previous work has been done in a semi-quantitative way by using different kinds of simplifications such as the mean size approximation, a di-atomic model for cavity nucleation etc. The most general description of cluster evolution can be achieved in the framework of a mean field approach, which is based on solution of the so-called Master Equation (ME). The numerical solution of ME, which essentially corresponds to a large number of differential equations, is a complicated computational problem. Indeed, for practical purposes, it is necessary to consider clusters containing a large number of point defects/atoms, thus the number of equations that need to be solved is normally too large to be used in numerical calculations. This is the case even for such simple point defect clusters as voids and dislocation loops when the size distribution function (SDF) depends on a single parameter, which is the number of defects in the clusters [25]. In the case of gas-vacancy clustering the computational problem is much more complicated since the size distribution function is two dimensional: it depends on the number of vacancies as well as gas atoms in the clusters. However the ME can be solved by means of numerical methods using procedures, which allow a reduction of the number of equations significantly. The grouping method first developed by Kiritani [25] for the case of vacancy clustering driven by Ostwald ripening, was intended to provide such a procedure. However, it was shown in [26] that the method is not accurate because the grouping equations are not fully consistent with the original ME. It was found in [26] that for the case of 1-D ME the simplest but still accurate grouping method may be obtained when the size distribution function (SDF) within a group is approximated by a linear function. Such an approximation maintains the identity of the grouped ME with the original, while satisfying the conservation laws for both the total number of clusters and the total number of point defects accumulated in the clusters. In [27] the grouping method was generalized for the case of 2-D ME when cluster evolution is driven by Ostwald ripening only. The grouping method has further been generalized to take into account bubble migration and coalescence in [28]. Thus, within the framework of the generalized grouping method describing evolution of the clusters, equal accuracy can be obtained for the general case when the evolution is driven simultaneously by cluster interactions with mobile point defects, and by Brownian motion of the clusters.

In order to model the impact of He on cavity evolution one needs to identify the mechanisms responsible for He mobility and transport in a crystal under irradiation. Essentially there are only two main mechanisms of He diffusion: Diffusion of He in an interstitial configuration, or by a substitutional mechanism with the help of di-vacancies. In addition there are several mechanisms which provide gas transport, such as thermal and radiation-

induced evaporation of gas atoms from bubbles and so-called replacement, driven by kick-out of a helium atom from a '1He + 1vacancy cluster' via reaction with a single interstitial atom. It should be noted that helium atoms in helium-vacancy clusters (3-D bubbles) are likely to be transported in the crystal via Brownian motion of these clusters. This may cause cavity coarsening and at high temperatures may deposit some helium atoms on the grain boundaries. In the present study we take into account only one mechanism for He diffusion, namely the interstitial one. For the gas transport we use the replacement mechanism. A reason for such simplifications is the relatively low irradiation temperatures which are not high enough to provide the thermal evaporation of gas atoms and Brownian motion of cavities. For the same reason the vacancy mechanism of He migration is not included. Another reason is related to small doses and relatively low levels of He concentration accumulated during implantation which will be expected to lead to only a minor impact of radiation-induced resolution of He from bubbles. The ME equation describing the evolution of cavities under irradiation conditions was formulated on the basis of the assumptions listed above. The grouping method [26] is used for numerical calculations of cavity evolution in iron irradiated with alpha particles, neutrons and neutrons after He implantation at two temperatures, 323 K and 623 K. An outline of the model and a brief description of the grouping method are provided in Section 4.2. The set of material and irradiation parameters used in the calculations is found in 4.3, while the results of the calculations are presented in Section 4.4.

4.2 Outline of Modeling

To describe the evolution of He-vacancy clusters driven by reactions with mobile point defects, the following ME has to be solved in a two-dimensional phase space of x, m (x and m are the number of vacancies and He atoms, respectively)

$$\frac{df(x,m)}{dt} = K_v(x) - \left(\nabla_x J_x(x,m,t) + \nabla_m J_m(x,m,t) \right), \qquad (6)$$

where $f(x,m)$ is the size distribution function (SDF) of He-vacancy clusters and $J_x(x,m)$, $J_m(x,m)$ are fluxes of clusters in x and m-space, respectively. The first term on the right hand side describes nucleation of small clusters during cooling down phase of cascades and is related to the fraction of vacancies, ε_v, which take part in vacancy agglomeration during cooling down of cascades. The nucleation rate $K_v(x)$, which in the following is considered as a fitting function which has to satisfy to the following equation

$$\sum_{2}^{\infty} x K_v(x) = \varepsilon_v G_{NRT} \left(1 - \varepsilon_r \right). \qquad (7)$$

G_{NRT} in Eq. (7) is the generation rate of defect production calculated in accordance with NRT standard and ε_r is a fraction of defects which recombine during cooling down of cascades. The second term on the right hand side of Eq. (6) describes cluster evolution driven by cluster interaction with point defects (∇_x, ∇_m are divergences in x and m space, respectively).

The fluxes are determined by the reactions of clusters with mobile defects and may be presented as follows

$$J_x(x,m) = P_x(x,m)f(x,m) - Q_x(x+1,m)f(x+1,m)$$

$$- Q_x^g(x+1,m)f(x+1,m), \tag{8}$$

$$J_m(x,m) = P_m(x,m)f(x,m) - Q_m(x,m+1)f(x,m+1),$$

where the coefficients $P_x(x,m)$, $Q_x(x,m)$, $P_m(x,m)$, $Q_m(x,m,t)$ and $Q_x^g(x+1,m)$ are the cluster reaction rates with mobile defects (vacancies, SIAs, mobile He atoms and SIA clusters) providing their growth (P) and shrinkage (Q). Note that for the sake of simplicity all SIA cluster are considered to have a size equal to 1, i.e. we treat them as crowdions.

A ME in the form of Eq. (6) is a set of rate equations for the density of clusters of different sizes in the range of practical interest. As mentioned above, it is necessary to consider clusters containing such a large number of vacancies and He atoms that the numerical solution of Eq. (6) becomes practically impossible. The grouping method developed in [25 - 28] permits the number of equations to be reduced substantially, thus providing a tool which can be used for numerical calculations. The main idea of the grouping method is that the xm phase space is divided into a series of groups with widths $\Delta x_i = x_i - x_{i-1}$, $\Delta m_j = m_j - m_{j-1}$, which include the clusters of the sizes $x_i = x_{i-1} + k$ ($k = 1, 2..., \Delta x_i$), $m_j = m_{j-1} + n$ ($n = 1, 2..., \Delta m_j$) and the SDF is approximated by a linear function within a group as follows

$$f_{i,j}(x,m) = L_0^{i,j} + L_{1x}^{i,j}(x - <x>_i) + L_{1m}^{i,j}(m - <m>_j), \tag{9}$$

where

$$<x>_i = x_i - \frac{1}{2}(\Delta x_i - 1),$$
$$\tag{10}$$
$$<m>_j = m_j - \frac{1}{2}(\Delta m_j - 1)$$

are mean cluster sizes within the ij group. In Eq. (9) the subscript i indicates the number of a group in x-space and the subscript j indicates the number of a group in m-space. Thus within the grouping method one needs to calculate three coefficients $L_0^{i,j}, L_{1x}^{i,j}, L_{1m}^{i,j}$ for each group instead of number of equations equal to $n_{i,j} = \Delta x_i \Delta m_j$ required by Eq. (6).

It has been shown [26 - 28] that the simplest accurate form of the equations for the coefficients $L_0^{i,j}, L_{1x}^{i,j}, L_{1m}^{i,j}$ can be derived assuming that the reaction rates with mobile defects for all cluster sizes within a group are equal.
In this case, equations for the coefficients $L_0^{i,j}, L_{1x}^{i,j}, L_{1m}^{i,j}$ are given by

$$\frac{dL_0^{i,j}}{dt} = \sum_{\lambda=x_{i-1}+1}^{x_i} K_v(\lambda) + \frac{1}{\Delta x_i}\left[J_x(x_{i-1}, <m>_j) - J_x(x_i, <m>_j)\right]$$
$$\tag{11}$$
$$+ \frac{1}{\Delta m_j}\left[J_m(<x>_i, m_{j-1}) - J_m(<x>_i, m_j)\right],$$

$$\frac{dL_{1x}^{i,j}}{dt} = -\left(\frac{\Delta x_i - 1}{2\sigma_i^2 \Delta x_i}\right)\left\{J_x(x_{i-1}, <m>_j) + J_x(x_i, <m>_j)\right.$$

$$\left. -2J_x(<x>_i - \tfrac{1}{2}, <m>_j)\right\}$$

$$+\frac{1}{\Delta m_j}\left\{\left[J_m(<x>_i + 1, m_{j-1}) - J_m(<x>_i, m_{j-1})\right]\right.$$

$$\left. -\left[J_m(<x>_i + 1, m_j) - J_m(<x>_i, m_j)\right]\right\}, \tag{12}$$

$$\frac{dL_{1m}^{i,j}}{dt} = -\left(\frac{\Delta m_j - 1}{2\sigma_j^2 \Delta m_j}\right)\left\{J_m(<x>_i, m_{j-1}) + J_m(<x>_i, m_j)\right.$$

$$\left. -2J_m(<x>_i, <m>_j - \tfrac{1}{2})\right\}$$

$$+\frac{1}{\Delta x_i}\left\{\left[J_x(x_{i-1}, <m>_j + 1) - J_x(x_{i-1}, <m>_j)\right]\right.$$

$$\left. -\left[J_x(x_i, <m>_j + 1) - J_x(x_i, <m>_j)\right]\right\}, \tag{13}$$

where

$$\sigma_i^2 = \frac{1}{\Delta x_i}\left[\sum_{\lambda = x_{i-1}+1}^{x_i} \lambda^2 - \frac{1}{\Delta x_i}\left(\sum_{\lambda = x_{i-1}+1}^{x_i} \lambda\right)^2\right],$$

$$\sigma_j^2 = \frac{1}{\Delta m_j}\left[\sum_{\lambda = m_{j-1}+1}^{m_j} \lambda^2 - \frac{1}{\Delta m_j}\left(\sum_{\lambda = m_{j-1}+1}^{m_j} \lambda\right)^2\right]. \tag{14}$$

Eqs. (14) give dispersions of cluster sizes in the *ij* group. Note that in the case when the group widths are taken to be equal to 1, i.e. $\Delta x_i = \Delta m_j = 1$, Eq. (11) is transformed to Eq. (6) since in the case $x_i = <x>_i$, $m_j = <m>_j$ (see Eqs. (10)) thus $f(x,m) = L_0^{ij}$ as can be seen from Eq. (9). Eqs. (12) and (13) have to be omitted in the case. In other words, there are no boundary problems between small size clusters, which are normally described by Eq. (6) ($\Delta x_i = \Delta m_j = 1$), and the bigger ones when $\Delta x_i > 1$, $\Delta m_j > 1$.

Eqs. (11) - (13) represent ME within the grouping method and may be used to describe cluster evolution during irradiation or ageing. As can be seen from these equations, the basic values which determine the cluster evolution are the fluxes $J_x(x,m)$, $J_m(x,m)$ in the *x, m* space.

In order to describe the evolution of He-vacancy clusters one needs to specify the fluxes $J_x(x,m)$, $J_m(x,m)$, to set up the equations for mobile point defects and also the initial and boundary conditions. It turns out [27, 28] that for the case where concentrations of 1-D SIA clusters and 3-D diffusing point

defects, $C_v(t), C_i(t), C_g(t), C_{He}(t)$, are measured in atomic fractions the rates $P_{x,m}(x)$ and $Q_{x,m}(x,m)$ may be written as follows

$$P_x(x) = wx^{\frac{1}{3}}D_vC_v(t),$$

$$Q_x(x,m) = Q_x^i(x,m) + Q_x^v(x,m) + Q_x^g(x),$$

$$Q_x^i(x,m) + Q_x^v(x,m) = wx^{\frac{1}{3}}\left[D_iC_i + D_v\exp\left(-E_v^b(x,m)/k_BT\right)\right]$$

$$Q_x^g(x) = 2\sqrt{\frac{k_g^2}{2}}D_gC_g\left(\frac{3\sqrt{\pi}\Omega}{4}\right)^{2/3}x^{2/3}, \tag{15}$$

$$P_m(x) = wx^{\frac{1}{3}}D_{He}C_{He},$$

$$Q_m(x,m) = \mu_R^{He}D_iC_if(x,m)\delta(x-1)\delta(m-1)$$

$$+wx^{\frac{1}{3}}D_{He}\exp\left(-E_{res}(x,m)/k_BT\right),$$

where $w = \left(48\pi^2/\Omega^2\right)^{1/3}$, D_v, D_i, D_{He} and D_g are the diffusion coefficients of 3-D diffusing vacancies, interstitials, He atoms in interstitial configuration and interstitial clusters; $E_v^b(x,m)$, $E_{res}(x,m)$, are the binding energies of vacancies and He atoms to a cluster of size x and containing m gas atoms, respectively; k_B is the Boltzmann constant and T the absolute temperature. $Q_m(x,m,t)$ is used here in the form similar to that for vacancies; $C_{He}(t)$ is the concentration of mobile He atoms. The value k_g^2 is the total sink strength for the 1-D diffusion of SIA clusters, which is given by [29]

$$k_g^2 = 2\left(\frac{\pi\rho_d d_{abs}}{4} + \chi_v\right)^2, \tag{16}$$

where ρ_d and d_{abs} are the density of dislocations and their capture diameter for the absorption of glissile SIA clusters, χ_v is the capture efficiency of voids for the glissile SIA clusters. The capture efficiency of voids, χ_v, can easily be calculated using the SDF

$$\chi_v = \sum_{x=2}^{\infty}\sum_{m=0}^{\infty}Q_x^g(x)f(x,m) + Q_x^g(1)\sum_{m=1}^{m_0}f(1,m), \tag{17}$$

where m_0 is the maximum number of He atoms associated with a single vacancy. The equation of state for He may be presented in the form $p(x,m) = \left(k_BT/\Omega\right)\left(m/x\right)Z(m/x,T)$ thus the binding energy of vacancies to the clusters in Eq. (15), $E_v^b(x,m)$, is given by

$$E_v^b(x,m) = E_v^f - \alpha x^{-1/3} + \left(m/x\right)Z(m/x,T)k_BT, \tag{18}$$

where E_v^f is the vacancy formation energy, $\alpha = 2\gamma\left(4\pi\Omega^2/3\right)^{1/3}$, γ is the surface energy and Ω is the atomic volume. The compressibility factor, $Z(m/x,T)$, is computed by using the expression derived by Manzke et al. [30] and Trinkaus [31]

$$Z(m/x,T) = (1-\rho)(1+\rho-52\rho^2) + \frac{b}{V_m}\rho(1-\rho)^2 + Z_m\rho^2(3-2\rho), \qquad (19)$$

where

$$\rho = \left(\frac{V_m}{\Omega}\right)\frac{m}{x},$$

$$V_m = 56T^{-1/4}\exp(-0.145\ T^{1/4}), \qquad\qquad (20)$$

$$Z_m = 0.1225\ V_m T^{\ 0.555},$$

$$b = 170T^{-1/3} - 1750T^{-1}.$$

In Eq. (20) V_m is the He atom volume, which is measured in cubic angstroms, and T is the temperature in K. Note that Eqs. (20) are written assuming that the volume of the cluster containing x vacancies, V, is equal to $V = x\Omega$.

Taking into account Eqs. (8), the evolution of mobile defect concentrations $C_v(t), C_i(t), C_{He}(t), C_g(t)$ may be presented as follows

$$\frac{dC_v}{dt} = G_v + Q_m(1)f(1,1) + Q_x(2,0)f(2,0) + \sum_{x=2}^{\infty}\sum_{m=0}^{\infty}Q_x^v(x+1,m)f(x+1,m)$$

$$-\mu_R D_i C_i C_v - \mu_R^{He}D_{He}C_{He}C_v - D_v(C_v - C_{vo})Z_v\rho_d \qquad (21)$$

$$-P_x(1)f(1,0) + \sum_{x=1}^{\infty}\sum_{m=0}^{\infty}P_x(x)f(x,m),$$

$$\frac{dC_i}{dt} = G_i - \mu_R D_i C_i C_v - D_i C_i Z_i \rho_d$$

$$-\sum_{x=2}^{\infty}\sum_{m=0}^{\infty}Q_x^i(x)f(x,m) - Q_x^i(1)\sum_{m=1}^{m_0}f(1,m), \qquad (22)$$

$$\frac{dC_{He}}{dt} = G_{He} + \sum_{x=2}^{\infty}\sum_{m=1}^{\infty}Q_m(m)f(x,m) + \sum_{m=1}^{m_0}Q_m(m)f(1,m) + \mu_R^{He}D_i C_i f(1,1)$$

$$-D_{He}C_{He}Z_{He}\rho_d - \mu_R^{He}D_{He}C_v C_{He} - \sum_{x=2}^{\infty}\sum_{m=0}^{\infty}P_m(x)f(x,m) - P_m(1)\sum_{m=1}^{m_0-1}f(1,m), \qquad (23)$$

$$\frac{dC_g}{dt} = G_g - D_g C_g k_g^2. \qquad (24)$$

where G_v, G_i, G_{He}, G_g are the generation rates of vacancies, self interstitial atoms (SIAs), He atoms and SIA clusters, respectively. μ_R is the coefficient describing the recombination reaction between SIA and vacancy, μ_R^{He} is the coefficient describing the reaction between a He atom and a vacancy and between a SIA and the He-vacancy cluster, $f(1,1)$; Z_v, Z_i are the capture efficiencies of dislocations for vacancies and SIAs, respectively, ρ_d is the dislocation density and C_{v0} is the thermal equilibrium vacancy concentration. The term $\mu_R^{He}D_i C_i f(1,1)$ in Eq. (23) describes the so-called displacement mechanism, i.e. the reaction $(He-vacancy) + SIA \rightarrow He$, which plays an

important role in He-vacancy cluster evolution allowing He atom transport in a crystal during irradiation.

The generation rates of vacancies, SIAs and SIA clusters are given by

$$G_v = G_{NRT}(1 - \varepsilon_r)(1 - \varepsilon_v),$$

$$G_i = G_{NRT}(1 - \varepsilon_r)(1 - \varepsilon_i^g), \qquad (25)$$

$$G_g = G_{NRT}(1 - \varepsilon_r)\varepsilon_i^g,$$

where G_{NRT} is the generation rate calculated using the NRT standard, and $\varepsilon_r, \varepsilon_v, \varepsilon_i^g$ are the fractions of the point defects recombined during the cooling down phase of cascades, the fraction of vacancies generated in the form of vacancy clusters and the fraction of SIAs generated in the form of glissile SIA clusters, respectively.

The set of Eqs. (11) - (13) together with the equations for the mobile defects has been numerically integrated using the Gear method. The calculations have been performed for the cases of neutron irradiation, alpha particle irradiation and neutron irradiation after alpha particle irradiation. In the case of neutron and alpha particle irradiations the initial conditions for the mobile defects and initial and boundary conditions for the SDF are taken in the following form

$$C_v(t)|_{t=0} = C_{v0},$$

$$C_i(t)|_{t=0} = C_{He}(t)|_{t=0} = 0,$$

$$f(x,m,t)|_{t=0} = C_{v0}\delta(x-1)\delta(m), \qquad (26)$$

$$f(x,0,t)|_{x=1} = C_v(t), \quad f(x,m,t)|_{x=\infty} = 0.$$

In Eq. (26) $\delta(x)$ is the Kronecker delta. The initial conditions for mobile defects in the case of neutron irradiation after alpha particle irradiation are taken from Eqs. (21) - (24) whereas the initial conditions for SDF are taken from what was calculated for the alpha particle irradiation.

4.3 Parameters used in the calculations

The calculations in the present work have been performed by numerical integration of Eqs. (11) - (13) and corresponding rate equations for the mobile defects, i.e. for vacancies, SIAs, SIA clusters and He atoms in interstitial configuration. Irradiation parameters used in the calculations are given in Table 6.

In all cases, except a few which are specifically mentioned, the same rates are used in the calculations. This means that generally $G_{He}/G_{NRT} = 6.5x10^3$ appm/dpa (about 154 FP per He atom). Maximum dose due to neutron irradiation is equal to 0.23 dpa; maximum dose due to He implantation is equal to 1.54×10^{-2} dpa, for 100 appm He.

Table 6. Implantation and displacement damage rates used in general in the modeling at temperatures of 323 or 623 K. The rates are the same as those used experimentally for specimens implanted with He and irradiated with neutrons.

Implantation ID	He implant G_{He} (appm/s)	He implant G_{NRT} (dpa/s)	Neutron irradiation G_{NRT} (dpa/s)	$T_{imp} = T_{irr}$ (K)	Implantation Time (s)
#1	6×10^{-4}	0.92×10^{-7}	5×10^{-8}	323	1.66×10^5
#2	1.8×10^{-3}	2.76×10^{-7}	5×10^{-8}	323	5.55×10^4
#3	6×10^{-3}	0.92×10^{-6}	5×10^{-8}	323	1.66×10^4
#4	1.2×10^{-3}	1.84×10^{-7}	5×10^{-8}	623	8.33×10^4
#5	3.6×10^{-3}	5.52×10^{-7}	5×10^{-8}	623	2.77×10^4
#6	1.2×10^{-2}	1.84×10^{-6}	5×10^{-8}	623	8.33×10^3

Material and other parameters used in our calculations are summarized in Table 7. As can be seen from Table 7 the number of parameters involved in the calculations is quite large. Some of them are known whereas others have to be considered as fitting parameters. Particularly, the effective vacancy migration energy E_v^m and cascade parameters, $\varepsilon_r, \varepsilon_i^g$, which play an important role in the modeling of cavity nucleation and growth, are considered here as fitting parameters. The vacancy migration energy is obtained by fitting calculated results to experimental data for cavity evolution during neutron irradiation at about room temperature. The parameters $\varepsilon_r, \varepsilon_i^g$ for the case of neutron irradiation are taken to be similar to those found in [29] by fitting calculation results to the experimental data for the swelling in neutron irradiated Cu. Such a choice is based on the results of MD simulations of cascades showing a quite similar behavior of cascades for Cu and Fe. The choice of the parameters $\varepsilon_r, \varepsilon_i^g$ for the case of He implantation is partly based on MD simulations of cascades and partly by considering them as the fitting parameters.

Table 7. Material parameters and irradiation and implantation parameters used in the present calculations. Parameter values used in the case of helium implantation are indicated by (He); those for neutron irradiation by (n).

Temperature, T	323 K, 623 K
Lattice parameter, a	0.2876 nm
Atomic volume , $\Omega = a^3/2$	1.189×10^{-29} m^3
Surface energy	1.95 J/m^2
Fraction of PD recombined in cascades, ε_r	0.90 (n); 0.5 (He)
Fraction of SIAs in cluster form, ε_i^g	0.25 (n); 0.05 (He)
Fraction of vacancies in cluster form, ε_v	See text
Recombination coefficients, $\mu_R = \mu_R^{He}$	1.0×10^{21} m^{-2}
Vacancy formation energy, E_v^f	2.12 eV
Vacancy diffusion coefficient, D_v - pre-exponential factor - migration energy, E_v^m	5.0×10^{-5} m^2/s 0.9 eV
SIA diffusion coefficient, D_i - pre-exponential factor - migration energy, E_i^m	1.0×10^{-6} m^2/s 0.06eV
SIA cluster diffusion coefficient, D_g - pre-exponential factor - migration energy, E_g^m	1.0×10^{-6} m^2/s 0.06eV
He diffusion coefficient, D_{He} - pre-exponential factor - migration energy, E_{He}^m	1.0×10^{-6} m^2/s 0.05eV
Dislocation density, ρ_d	10^{13} m^{-2}
Maximal number of He atoms in vacancy, m_0	4
Dislocation capture efficiencies for vacancies and SIAs, Z_v, Z_i	1.00, 1.04
Dislocation capture diameter for SIA clusters, d_{abs}	7 nm

4.4 Results of the calculations

4.4.1 Neutron irradiation at 323K

To calculate nucleation and growth of vacancy clusters (cavities) under irradiation one has to use the migration and formation energy of vacancies.

Particularly vacancy migration energy plays a very important role for homogeneous nucleation mechanism which is considered to operate at low temperatures. There is a big uncertainty regarding the value of the migration energy E_v^m in iron – one can find values in the literature that varies from about 0.55 to 1.2 eV. Recent ab-initio calculations [32] revealed the value of $E_v^m = 0.67$ eV. This value was taken firstly for the calculations of the cavity evolution in neutron irradiated iron at 323K. The results obtained are presented in Fig. 15 (see blue curve) together with the experimental data and results of the calculations obtained under different conditions. As can be seen from the plot the calculated void density in the case of $E_v^m = 0.67$ eV is much lower than the experimental results. Moreover our calculations have shown that this result essentially does not change by varying other parameters except vacancy migration energy. Close examination shows that the reason for this discrepancy is related to high vacancy mobility, which restricts the cavity nucleation rate by lowering the vacancy steady state concentration. This is illustrated in Fig. 16 which shows the strong sensitivity of mobile vacancy concentration to the assumed vacancy migration energy. Thus, to obtain a fair agreement between experimental values and calculations (Fig. 15), we are led to accept a vacancy migration energy of about 0.9 eV. However, the calculated cavity density still remains smaller than the experimental value at the lowest dose of 10^{-4} dpa. This cannot be improved by further increase of E_v^m because at $E_v^m > 0.9$ eV vacancies become practically immobile. Therefore cavity nucleation at small doses drops down in the case when $E_v^m > 0.9$ as seen in Fig. 15 where the calculated results for $E_v^m = 1.0$ eV are also presented. Thus in the following calculations the value of an effective vacancy migration energy is taken to be equal to 0.9 eV.

The reason for the deviation between the calculations and experiment at the lowest dose is not clear. The difference between experiments and calculations may be related to an additional nucleation mechanism or to an overestimate of the cavity density at low doses by the PAS technique. To test the first case, calculations have been carried out taking into account a possibility of cascade cavity nucleation. The green dotted line in Fig. 15 has been calculated using a cascade assisted mechanism of void nucleation with the supposition that 10% of vacancies are clustered into small cavity nuclei during cooling down of the displacement cascades ($\varepsilon_v = 0.1$). As can be seen from the plot an impact of the mechanism is very small at low doses. On the other hand the cavity density estimated by PAS may be somewhat overestimated due to the presence of dislocation loops [18].

The nucleation rate, $K_v(x)$ (Eq. (7)) is chosen in the following form.

$$K_v(x) = \begin{cases} A / x^n, & x \le 15, \quad (n = 1 - 2), \\ 0, & x > 15, \end{cases} \tag{27}$$

where the parameter A is calculated from Eq. (7). Our calculations show that the main impact on void nucleation due to $K_v(x)$ comes from the magnitude of the fraction ε_v whereas the parameter n plays a minor role. Hence, the calculation presented in Fig. 15 is done with n=1.

All calculations discussed above have been done in the framework of the PBM (see e.g. [33]) assuming that 25% of interstitials are contained in small glissile clusters formed already during the cooling down phase of cascades. These small clusters/loops diffuse one-dimensionally. Another possibility is to make the calculations within the framework of Standard Rate Theory, i.e. for $\varepsilon_i^g = 0$. The results of such calculations are also presented in Fig. 15 (see the yellow and brown dash-dotted curves). As can be seen the calculated cavity density stays well below the experimental data even when the dislocation bias was varied by an order of magnitude. On the other hand the calculations made by using PBM allow one to explain both the dose dependence of cavity density and vacancy accumulation. Indeed as can be seen in Fig. 17 the dose dependence of cavity size distribution function agrees quite well with the experimental observations reported in Fig. 4 in [7]. Thus one may conclude that cascade clustering of SIAs and their 1-D transport is a crucially important mechanism in iron under neutron irradiation.

4.4.2 He implantation at 323K

He-vacancy cluster evolution in the case of helium implantation at 323 K has been calculated within the framework of PBM with cascade parameters given in Table 7. The calculations have been carried out for the three irradiation conditions described in Table 6. It has been found that accumulation of the clusters in this case is quite different from that observed during neutron irradiation. Indeed as can be seen from Figs. 17 and 18 the sizes of the clusters in the case of He implantation are much smaller than the ones calculated for neutron irradiation. There are two reasons which may be responsible for this: (a) much higher generation rate of point defects during He implantation than during neutron irradiation and (b) very low level of irradiation dose. It can easily be seen by comparing the dose dependence of point defect concentrations calculated for the neutron irradiation (Fig. 16) with that for He implantation (Fig. 19). In contrast to the neutron irradiation, the steady state concentration of vacancies at the He implantation regime builds up at essentially higher level that takes place at a dose of about 10^{-2} dpa, i.e. very close to the end of implantation. Thus practically during a course of implantation vacancy supersaturation is negative that prevents growth of the clusters.

In Fig. 20 the dose dependence of the cluster density calculated is presented for different implantation rates. As can be seen from the plot, accumulations of cluster densities are very close to each other. Moreover they are somewhat similar to those calculated for neutron irradiation. This shows that the homogeneous mechanism of vacancy cluster nucleation at this temperature is so powerful that the presence of He plays a minor role in the nucleation. The only difference is that a major part of the clusters in the case of He implantation contains He atoms. Moreover the He density in the clusters is extremely high (on average more than one He atom per vacancy). Because the positron lifetime is sensitive to the actual free volume in vacancy clusters, it is not surprising that the mean positron lifetime in the He implantation case is found to be smaller than in the case of neutron irradiation (see Fig. 4a).

4.4.3 Neutron irradiation at 623K

Cavity evolution in the case of neutron irradiation at 623 K has been calculated using the same set of parameters as used for the low temperature neutron irradiation. The first calculations have been done taking into account the homogeneous cavity nucleation only, similar to the case of the low temperature irradiation. It has been found that this mechanism does not allow a high enough nucleation rate to build up cluster densities comparable with the experimental observations. However it can be done by taking into account intra-cascade vacancy clustering, i.e. by assuming that $\varepsilon_v \neq 0$. The results of the calculations for the case $\varepsilon_v = 0.1$ are presented in Fig. 21 and 22. The dose dependence of the point defect concentration is presented in Fig. 21. As can be seen, mobile defect concentrations obey the typical sink regime: the fast diffusing defects, SIAs and SIA clusters, reach their steady state values at very low doses and practically remain constant up to the doses when the cavity sink strength becomes high enough to compete with that of dislocations. The difference between the concentration behavior of SIAs and SIA clusters, i.e. a shift of the SIA cluster concentration to higher doses and higher value compared to that of SIA concentration, is related to the difference in sink strengths of voids and dislocations for the 1-D (SIA clusters) and 3-D (SIAs) diffusing defects.

Dose dependences of the calculated density and size of the clusters are presented in Fig. 22 together with the experimental values. As can be seen the calculated results agree qualitatively with the observations. However both the calculated density and size are higher than the measured ones. Especially the cluster size is considerably higher resulting in an order of magnitude higher swelling. The origin of the discrepancy is not clear yet. A possible explanation for this may be that the capture diameter of dislocations for the absorption of the SIA clusters, d_{abs}, is in reality smaller than that used for the calculations (see Table 7). Indeed the value listed in Table 7 was chosen by an analogy with Cu for which this value has been successfully used to describe swelling during neutron irradiation [29]. For the low temperature calculations given above this parameter is not important because the cavity size in that case is very small ($\sim 1nm$) compared to the saturation value for the cavity diameter of $d^{sat} \approx \pi d_{abs}$ (see e.g. [36, 37]), which is ~ 3 nm even at $d_{abs} = 1nm$. At a temperature of 623 K the situation is qualitatively different because the cavities in this case can grow to larger sizes. Thus the size saturation, which is caused by interaction between cavities and SIA clusters, can take place and may be responsible for the observed lowering of cluster size and swelling. The green curve in Fig. 22 corresponds to the case when the cluster evolution has been calculated with $d_{abs} = 1$ nm. As can be seen, the calculation in this case becomes closer to the experimental results. Maybe this result gives a light to understand the swelling resistance of iron and iron based alloys which could be an important topic for future investigations.

4.4.4 He implantation at 623K

As can be seen from Table 6, He implantation has been carried out at three different implantation rates with a constant ratio between He implantation rate and defect generation rate. The dose dependence of the density and mean size of He-vacancy clusters calculated for all three cases with $\varepsilon_v = 0$ are presented in Fig. 23 (intra-cascade vacancy clustering is not important in this case). As can be seen the number density of the clusters at this temperature is generally higher than that of the neutron irradiation (Fig. 22). There are two reasons for this: (a) higher defect generation rate and (b) helium impact on the cluster nucleation. Note that cavity nucleation in this case indeed is highly efficient - the terminal cluster density is comparable to the neutron case for comparable displacement damage rates even though the displacement dose is about an order of magnitude lower. Moreover, nucleation of clusters still continues in the implantation case whereas it tends to saturate at a dose level above 10^{-3} dpa in the case of neutron irradiation (see Fig. 22). Both calculated density and size of the clusters agree reasonably well with the experimental data obtained by PAS measurements, also presented in Fig. 23. The terminal SDF of He-vacancy clusters presented in Fig. 24 clearly shows that the cluster evolution is still in the nucleation regime- a large portion of the clusters have a size which is much smaller than that of the mean size. Note also that the calculations show that cluster nucleation under implantation conditions does not require the cascade production of small vacancy clusters as is the case for neutron irradiation. In other words, the cluster nucleation under the implantation conditions is driven mainly by the He.

There is a clear general trend of the calculated results shown in Fig. 23, namely that a decrease in He implantation rate results in a decrease in cavity density and an increase in size. Calculations for implantation rates down to 1.2×10^{-5} appm He/s demonstrate that this trend continues also for lower rates than shown in Fig. 23.

The dose dependence of mobile point defect concentrations calculated for the case of the highest He generation rate is presented in Fig. 25. As can be seen the steady state of vacancy concentration is reached at very low doses. The non monotonic behavior of the concentration of mobile He atoms (orange dash-dotted line) is due to the replacement mechanism of He transport. This mechanism which is responsible for the He concentration increase seen in the plot starts operating at very low doses. Thus the cluster evolution proceeds in a way that allows nucleation and growth of the clusters within quite a wide dose range.

It has to be emphasized that the calculated cluster size looks quite reasonable even though it is somewhat higher than that estimated by PAS (Fig. 23). Indeed the calculations show that the in-void pressure of He atoms during He implantation at 623 K is extremely high (the ratio of <m>/<x> is about 0.5), i.e. there is a strong driving force for cavity growth. In this respect the results obtained by TEM – no visible voids at all after implantation of 100 appm He (see paragraph 3.2.1) look very surprising. The reason for the discrepancy between the PAS results (and the calculations) and TEM results remains unclear.

As can be seen from Table 6 the He implantation has been done with extremely high He to damage ratio (i.e. about 6500 appm/dpa) which is orders of magnitude higher than the one expected in both fission and fusion reactors. However by use of the model described above one can try to estimate cavity evolution under the He implantation conditions expected in the reactors. The results of such calculations are presented in Fig. 26 (green curves) and compared with results presented in Fig. 23 for high He to damage ratio (red curves). To calculate the green curves in Fig. 26 the He implantation rate was taken to be equal to 10^{-5} appm/s and defect generation rate to $\sim 10^{-6}$ dpa/s (i.e. equivalent to 10 appm/dpa) that roughly corresponds to typical fusion reactor conditions. As seen from the plot, cavity nucleation in this case takes place only at the very beginning of irradiation and results in the cavity density of the order of 10^{20} m^{-3}. For the green plot in Fig. 26 the capture diameter of dislocation for 1-D SIA clusters was taken as $d_{abs} = 1$ nm, but the cavity density is only very slightly dependent on this parameter. Based on Fig. 26 one may conclude that the ratio between He implantation rate and defect generation rate is an important parameter which determines the ability of He atoms to maintain cavity nucleation.

4.4.5 Neutron irradiation after He implantation

Cavity evolution in iron under neutron irradiation after He implantation has been calculated using the cavity SDF obtained during He implantation as the initial conditions and the same radiation parameters used here for pure neutron irradiation. The calculations have been carried out for two temperatures: 323 K and 623 K. Fig. 27 shows the calculated SDF after He implantation to a concentration of 100 appm He at 323K (red curve). The terminal SDF in iron irradiated - also at 323 K - with neutrons to a dose of 0.23 dpa after the He implantation, is also presented (blue dashed curve). As can be seen the cavity growth is rather limited; the mean diameter increases to about 0.7 nm. This probably explains why the cavities have not been observed by TEM.

Fig. 28 shows the calculated mean 'in-cavity He density' at 323 K as a function of the mean number of vacancies in the cavities. The density first decreases and then increases with increasing He concentration, resulting in about 1.4 He/vacancy after implantation of 100appm He (red curve). The subsequent neutron irradiation (up to 0.23 dpa) further increases the mean number of vacancies in the cavities, resulting in a decrease of the average He density.

The terminal cavity 2-D SDFs calculated for the case of neutron irradiation to doses of 0.023 and dpa 0.23 dpa after He implantation (at 623 K) are presented in Figs. 29 and 30. Comparison of the SDFs in Figs. 29 and 30 with the one for 100 appm He implantation at 623 K (Fig. 24) shows that the cavity-SDF under neutron irradiation is subject to growth (see also Fig. 32 for comparison of the 1-D SDFs). As can be seen in Fig. 30 the terminal cavity diameter reaches a value of about 7 nm which is in fair agreement with the

PAS result (Table 3), but appreciably higher than the estimate by TEM (Table 4).

Figure 31, the equivalent (at 623 K) to Fig. 28 (at 323 K), shows the calculated mean 'in-cavity He density' as a function of the mean number of vacancies in the cavities during He implantation up to a concentration of 100 appm He (red curve) and subsequent neutron irradiation (up to 0.23 dpa). Qualitatively, the variation of the He/vacancy ratio is similar to the behaviour at 323 K, i.e. the ratio first decreases and then increases with increasing He concentration and subsequently decreases with neutron dose. However, the mean cavity volumes are roughly a factor of 1000 bigger at 623 K than at 323 K, while the He/vacancy ratio is of the same order of magnitude ($0.1 - 1$) at the two temperatures.

5. Summary and Conclusions

5.1 Experimental evaluation of microstructure

In accordance with our declared objective we have attempted to determine the size and density of cavities in pure iron and a ferritic steel (EUROFER 97) induced by helium implantation at 323 and 623 K. Measurements have been made in the as-implanted and in the implanted and subsequently neutron irradiated states. Both Positron Annihilation Spectroscopy (PAS) and Transmission Electron Microscopy (TEM) have been used to characterize the cavities. To illustrate the effects of implanted helium on cavity evolution, measured lifetime spectra are shown in Figs. 1-3 for pure iron and in Figs. 5-7 for EUROFER 97. These spectra were measured on specimens after implantation to different helium concentrations as well as after post-implantation neutron irradiation to different displacement damage levels at 323 and 623 K. The lifetimes and intensities of the lifetime components extracted from a number of measured spectra for specimens which were implanted and/or neutron irradiated at 623 K are shown in Table 1 and 2 for pure iron and EUROFER 97, respectively. The tables also include values of the mean positron lifetimes. The mean lifetimes are plotted against displacement dose level for as-implanted as well as for implanted and neutron irradiated specimens in Fig. 4 and Fig. 8 for pure iron and EUROFER 97, respectively.

The results obtained using PAS demonstrate clearly and consistently that the implantation of helium both in the as-implanted state as well as in the implanted and neutron irradiated condition has significant effects on the evolution of the cavity population. The data also illustrate the sensitivity of the results to parameters such as implantation and irradiation temperatures, concentration of implanted helium and level of displacement doses (arising from either the helium implantation or fission neutron irradiation). The PAS results show quite marked response of helium implantation on the evolution of helium bubbles which is very important in the process of trying to understand the role of implanted helium in damage accumulation.

As mentioned in Section 3, PAS is sensitive to vacancies, vacancy clusters (including voids) and the presence of He in the cavities. In principle this fact makes it possible to extract information on cavity sizes and densities as well as on He-to-vacancy ratios in the cavities ('He bubbles') [23]. In order to establish the correlation between measured positron lifetime spectra and defect characteristics it is necessary to know the quantitative dependence of the positron lifetime on cavity size and He-to-vacancy ratio in the cavities as well as the dependence of the specific trapping rate for positrons on the cavity size and He content. These dependencies are associated with some uncertainties. Furthermore, it is possible to extract only a limited number of lifetime components from measured positron lifetime spectra. In most cases the defect microstructure consists of distributions of cavity sizes and He densities (Section 4). The experimentally extracted lifetime components should therefore be associated with some proper averages of these distributions. This averaging adds an extra uncertainty to the determination of the defect characteristics by PAS. However, by carefully considering the various uncertainties it is possible to obtain fair (semi-) quantitative estimates of cavity densities and average sizes from the PAS data.

Qualitatively, the observation of positron lifetime components with lifetimes in the range from about 250 to 500 ps in iron that has been either neutron irradiated, He implanted or neutron irradiated after He implantation at ~323 K [7, 13] and 623 K (Tables 1, 3) demonstrates the presence of cavities with sizes in the sub-nm range and bigger, and with high densities.

In addition to the PAS measurements also TEM investigations were carried out. In the specimens as-implanted with He at 323 K and in those which were neutron irradiated after He implantation at the same temperature no small (nm-sized) cavities were observed (although nm-sized voids have been observed previously [7, 38] after neutron irradiation to higher displacement doses than applied in the present study). However, a low density (~$2 \times 10^{19} m^{-3}$) of relatively large voids (~52 nm) were observed in iron specimens after implantation with 100 appm of helium and subsequent neutron irradiation to 0.1 dpa, both at 323 K (Fig. 13b and [13]). Even larger cavities with a similar density (~ 90 nm diameter, ~$1 \times 10^{19} m^{-3}$) were observed after neutron irradiation to a rather low dose of 0.036 dpa (Fig. 13a).

For iron specimens which were neutron irradiated at 623 K (i.e. well above recovery stage V) with or without prior helium implantation nm-sized cavities are clearly observed by TEM. On the other hand, no cavities were resolved by TEM in specimens that had been only helium implanted (i.e. without neutron irradiation) even at the high temperature of 623 K.

Thus, generally the advantage of applying both techniques, PAS and TEM, for the characterization of the cavity microstructure of He implanted and/or neutron irradiated iron is clear. PAS is able to resolve very small cavities that cannot be resolved by TEM, while on the other hand TEM is able to demonstrate the presence of large cavities of a density that is too low to allow detection by PAS. In the intermediate size range, results obtained by the two techniques can be compared quantitatively (Tables 3 and 4). Although not

exactly identical, the results of PAS are in reasonably good agreement with the TEM results where comparisons can be made (the most extreme difference being observed for iron implanted with 100 appm of helium at 623 K and subsequently neutron irradiated at 623 K to 0.23 dpa. The reason for this disagreement is not clear). Thus it can be concluded that the use of these two techniques makes it possible to study the evolution of helium induced cavities in metals under different irradiation conditions.

5.2 Modeling and comparison with experimental results

The second objective of the present task has been addressed in quite some detail in Section 4 where the evolution of helium-vacancy clusters into cavities has been treated under different irradiation conditions. In order to do it in a self consistent manner, we first considered the evolution of cavities under neutron irradiation at the low temperature of 323 K, i.e. well below the recovery stage V. As shown in Fig. 15 the cavity nucleation during neutron irradiation at 323 K is found to be very efficient leading to high cavity densities. The dose dependence of the cavity density in iron (without implanted helium) was calculated within the framework of homogeneous nucleation assuming vacancy diffusivity appropriate to yield the dose dependence of the cavity density at 323 K determined experimentally as shown in Fig. 15. The major parameters describing defect production under cascade damage conditions are also adjusted in calculating the dose dependence of cavity density. It should be emphasized that these parameters have been used in all our calculations of cavity population during neutron irradiation. Note that the cascade parameters, such as the cascade efficiency and magnitude of the SIA fraction taking part in SIA cluster formation, were chosen to be close to those obtained by fitting experimental data for neutron irradiated copper. Those parameters were found to be quite reasonable in the case of iron as well. Thus the MD results show that the difference between these two crystals with respect to the cascade properties under comparable PKE energies is not large.

In the study of the impact of helium on cavity evolution we considered first the evolution of helium-vacancy clusters during helium implantation at temperatures below and above the recovery stage V to different levels of helium concentrations. Further the evolution of the as-implanted microstructure was treated under neutron irradiation to different displacement dose levels at the implantation temperatures. The calculations were carried out using the PBM model including 1-D diffusion of SIA clusters produced in cascades and sub-cascades. Results of calculations are presented in Section 4.4 and wherever possible compared with the experimental results reported in Section 3.

In Fig. 22, for example, we compare the calculated cavity size and density with those measured mainly by TEM in neutron irradiated iron (without implanted helium) at 623 K. It can be seen that the experimental results agree quite well with the calculated ones. The size and density of cavities formed during implantation of helium to the levels of 10 and 100 appm at 623 K were

also calculated and are compared with values estimated from results of PAS measurements in Fig. 23.

Although there is a rather limited number of results from PAS and TEM which can be used for such *quantitative* comparisons, there is on the other hand, a significant volume of TEM and PAS results reported in Section 3 which can be used for at least *qualitative* comparisons with the calculated general trends of the effects of helium on cavity evolution during neutron irradiation. PAS measurements, for example, of positron lifetime spectra directly although qualitatively demonstrate that the cavity formation in iron both at 323 K and 623 K is enhanced by increasing displacement dose, decreasing irradiation temperature and increasing helium concentration. These rather important general tendencies are in qualitative agreement with the calculated results reported in Section 4.

5.3 Concluding remarks

The present experiments have demonstrated some rather remarkable effects of helium implantation and post-implantation neutron irradiation on cavity formation and growth in pure iron. These results are important from technological as well as academic points of view and therefore are worth highlighting. The results presented in Fig. 4(a) suggest, for example, that the level of cavity formation and growth in iron implanted at 323K with 100 appm of helium or He implanted and neutron irradiated (to ~0.01 dpa) does not exceed to any large extent the level of cavity nucleation and growth in neutron irradiated iron without helium implantation (see also Fig. 20). This implies that at this temperature the homogeneous nucleation of cavities is very efficient even in the absence of implanted helium. In other words, the presence of helium (implanted with the conditions used in the present experiments) would not be expected to play any significant role in the evolution of cavities during neutron irradiation at 323 K.

At 623K (i.e. temperature above the recovery stage V), on the other hand, the implanted helium does cause an increase in cavity nucleation and growth (Fig. 4(b)). This is because at this temperature, the implanted helium atoms help to stabilize the cavity nuclei against shrinkage by thermal evaporation of vacancies, which would take place in the absence of He. Consequently, both cavity nucleation and growth are enhanced. It is interesting to note here, however, that according to our calculations (section 4, Fig. 26) the enhancement in cavity nucleation and growth is unlikely to occur under the condition of a low ratio between helium generation rate and displacement damage rate (eg. 10 appm/dpa) and at a damage rate of 10^{-6} dpa/s as produced for example by 14 MeV neutrons in the first wall of a fusion reactor. As can be seen in Fig. 26, the experimentally determined cavity density in iron irradiated with fission neutrons at 623K without pre-implanted helium (broken line) (see Table 4) is considerably higher than what could be expected for a low ratio of helium concentration to damage level of 10 appm/dpa.

Traditional simulation experiments (including the present ones) often use helium implantation followed by neutron irradiation to simulate the effect during fusion-neutron irradiation of enhanced helium generation rate (relative to fission-neutron irradiation). However, the above discussion directly implies that such experiments may easily result in misleading effects on cavity evolution (see Fig. 26). This unfortunate situation arises simply because of the use of very high helium implantation rates to achieve large concentrations of implanted helium in relatively short times. The use of very high implantation rates leads to the formation of a highly dense population of helium induced cavities. This microstructure is very stable and controls the evolution of cavity microstructure during the following neutron irradiation. This is in contrast to the situation during fusion-neutron irradiation where the low generation rate of helium leads to only a small density of stable helium induced cavities compared to the density of cavities resulting from the displacement damage created by the neutron irradiation as illustrated in Fig. 26.

Acknowledgements

References

1   R.L. Klueh, K. Ehrlich and F. Abe, J. Nucl. Mater. 191 – 194 (1992) 116.
2   K. Ehrlich and K. Anderko, J. Nucl. Mater. 171 (1990) 139.
3   D.S. Gelles, J. Nucl. Mater. 212 – 215 (1994) 714; 233 – 237 (1996) 293.
4   J.M. Vitek, W.R. Corwin, R.L. Klueh and J.R. Hawthorne, J. Nucl. Mater. 141 – 143 (1986) 948.
5   V.S. Khabarov, A.M. Dvoriashin and S.I. Porolle, J. Nucl. Mater. 233 – 237 (1996) 236.
6   M. Eldrup and B.N. Singh, J. Nucl. Mater. 276 (2000) 269.
7   M. Eldrup, B.N. Singh, S.J. Zinkle, T.S. Byun and K. Farrel, J. Nucl. Mater. 307 – 311 (2002) 912.
8   B.N. Singh, Risø Report No. Risø-R-1422(EN), August 2003, p. 28.
9   B.N. Singh and J.H. Evans, J. Nucl. Mater. 226 (1995) 29.
10   H. Trinkaus and B.N. Singh, J. Nucl. Mater. 307 – 311 (2002) 900.
11   B.N. Singh and H. Trinkaus, J. Nucl. Mater. 186 (1992) 153.
12   B.N. Singh and T. Leffers, Radiation Effects 101 (1986) 73.

13 B.N. Singh, M. Eldrup, S.I. Golubov, D.J. Edwards and P. Jung, Risø Report No. Risø-R-1496(EN) (2005) 38 p.

14 P. Jung, "Helium implantation in pure iron and RAFM steels at <70 and 350°C". Task:TW4-TTMS-001a, EFDA Technology Programme (2004).

15 M. Eldrup and B.N. Singh, J. Nucl. Mater. 251 (1997) 132.

16 M. Eldrup, J. Phys. (Paris) IV Colloq. 5 (1995) C1-93.

17 K.O. Jensen and R.M. Nieminen, Phys. Rev. B 35 (1987) 8219.

18 M. Eldrup, Meimei Li, L.L. Snead and S.J. Zinkle, Nucl. Instr. and Meth. B 266 (2008) 3602.

19 M. Eldrup, Mat. Sci. Forum 105-110 (1992) 229.

20 J.V. Olsen, P. Kirkegaard, N.J. Pedersen and M. Eldrup, phys. stat. sol. (c) 4 (2007) 4004 and www.PALSfit.dk

21 M. Eldrup and B.N. Singh, Risø Report No. Risø-R-1241 (EN), December 2001.

22 A. Hempel, M. Saneyasu, Z. Tang, M. Hasegawa, G. Brauer, F. Plazaola, S. Yamaguchi, F. Kano and A. Kawai, p.560, in Effects of Radiation on Materials: 19th Int. Symposium, ASTM STP 1366 (Eds: M.L. Hamilton, A.S. Kumar, S.T. Rosinski and M.L. Grossbeck) 2000.

23 K.O. Jensen, M. Eldrup, B.N. Singh and M. Victoria, J. Phys. F 18 (1988) 1069.

24 B.N. Singh, Xiaoxu Huang, S. Tähtinen, P. Moilanen, P. Jacquet and J. Dekeyser, Risø Report No. Risø-R-1616(EN), November 2007.

25 M. Kiritani, J. Phys. Soc. Japan 35 (1973) 95.

26 S.I. Golubov, A.M. Ovcharenko, A.V. Barashev, and B.N. Singh, Philos. Mag. Series A. 81, No.3 (2001) 643-658.

27 S.I. Golubov, R.E. Stoller, S.J. Zinkle, Fusion Materials Semiannual Progress Report, 2002, DOE/ER-0313/33, US Department of Energy, 155.

28 S.I. Golubov, R.E. Stoller, S.J. Zinkle, Fusion Materials Semiannual Progress Report, 2003, DOE/ER-0313/35, US Department of Energy, 214.

29 S.I. Golubov, B.N. Singh, H. Trinkaus, Philos. Mag. A 81 (2001) 2533.

30 R. Manzke, W. Jäger, H. Trinkaus, G. Crecelius, R. Zeller, Solid State Commun. 44 (4) (1982) 481.

31 H. Trinkaus, Radiation Effects 78 (1983) 189.

32 Chu-Chun Fu and F. Willaime, Physical Review B 72, (2005) 064117.

33 H. Trinkaus, B.N. Singh, A.J.E. Foreman, J. Nucl. Mater. 199 (1992) 1.

34 A.M. Ovcharenko, S.I Golubov, C.H. Woo, Hanchen Huang, Computer Physics Communications 152, No.2 (2003) 208-226.

35 S.I. Golubov, R.E. Stoller, S.J. Zinkle, J. Nucl. Mater. 361 (2007) 149-159.

36 B.N. Singh, S.I. Golubov, H. Trinkaus, A. Serra, Yu.N. Osetsky, A.V. Barashev, J. Nucl. Mater. 251 (1997) 107-122.

37 A.V. Barashev, S.I. Golubov, J. Nucl. Mat. (2009) 407-409.

38 S.J. Zinkle and B.N. Singh, J. Nucl. Mater. 351 (2006) 269-284.

Figures
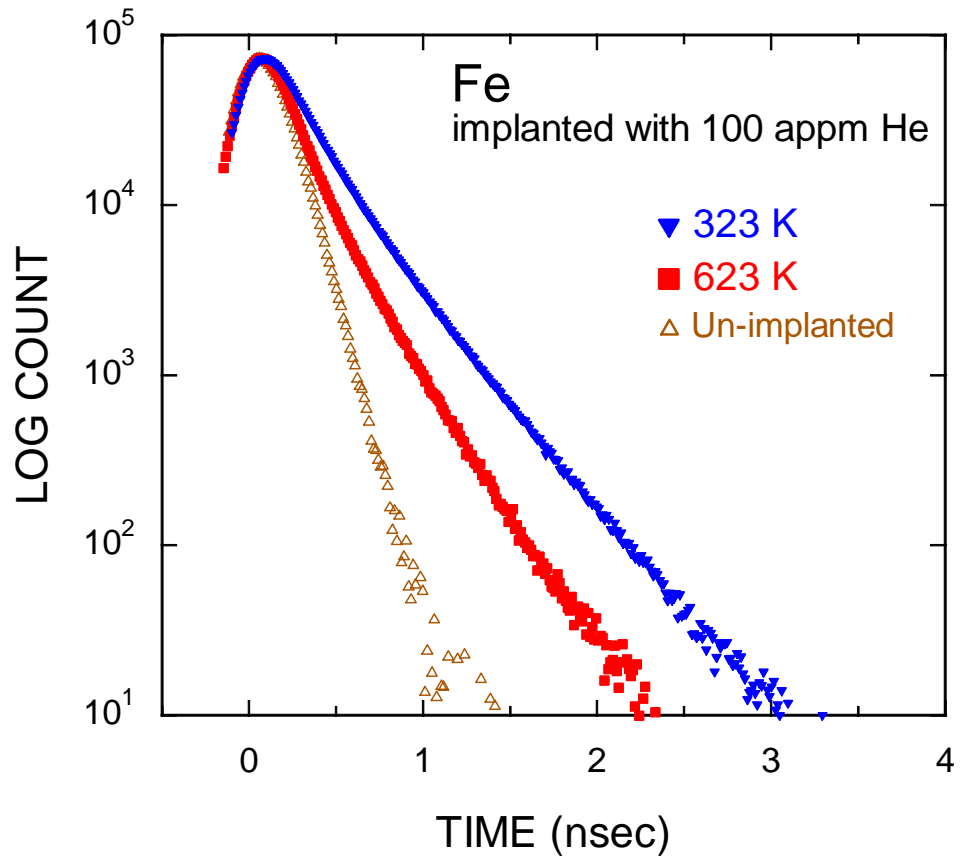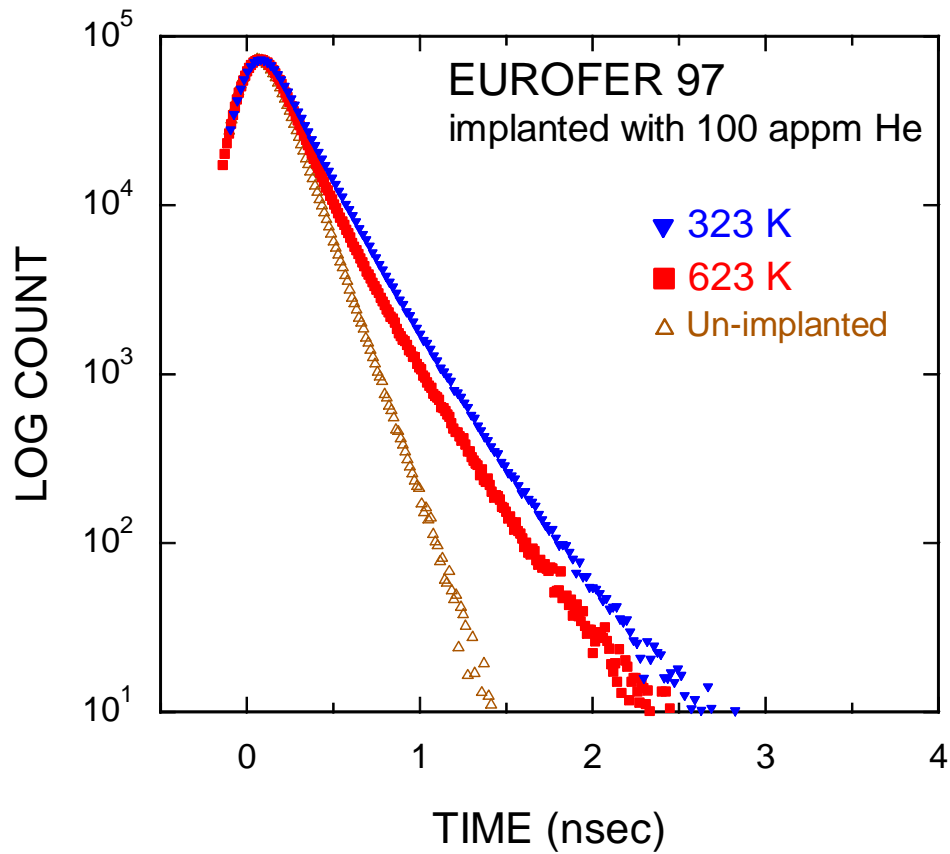

Figure 1. Positron lifetime spectra for Fe implanted with 100 appm of helium at 323 K and 623 K. The larger effect of implantation at 323 K than at 623 K is due the generation of a high density of small cavities at the lower temperature.
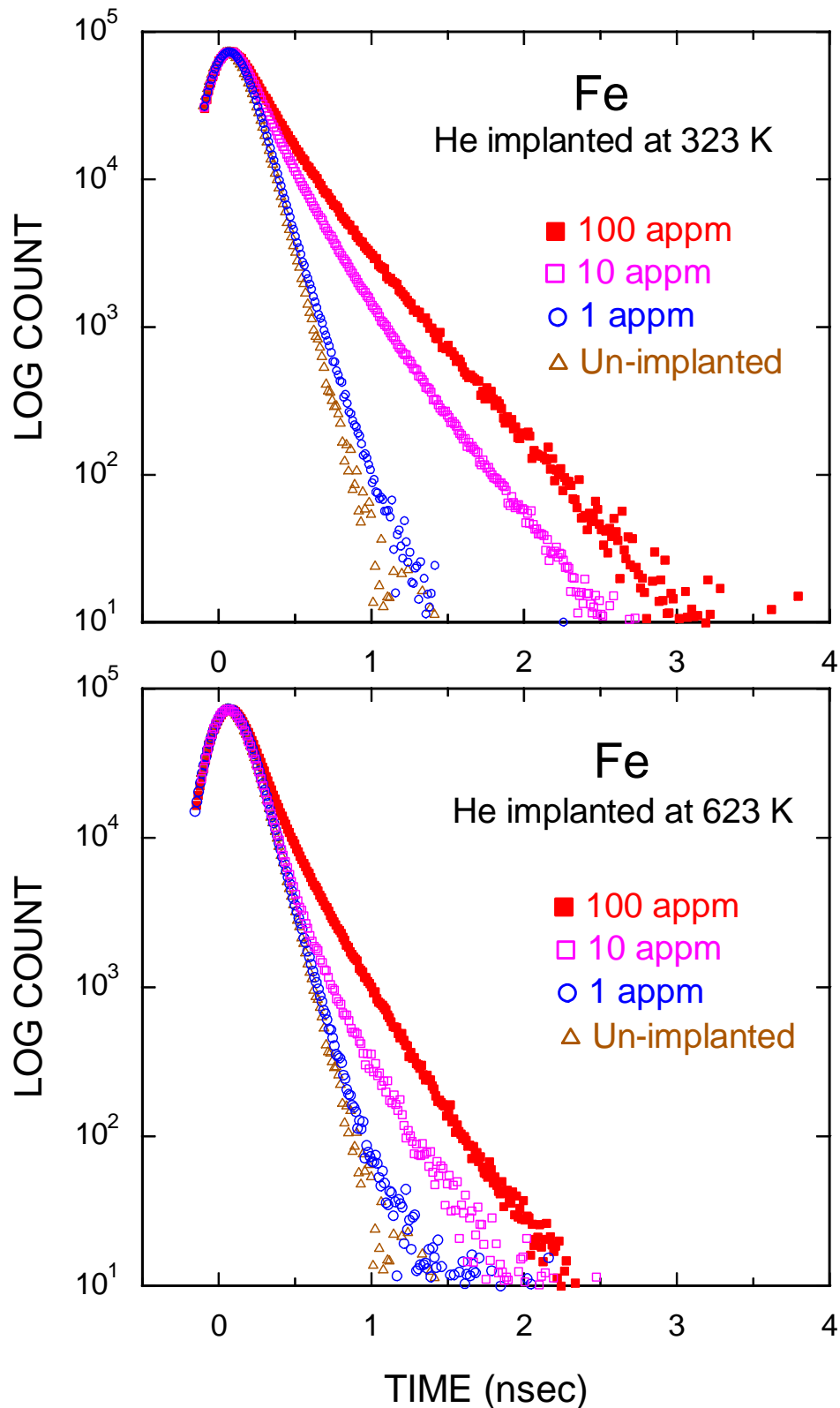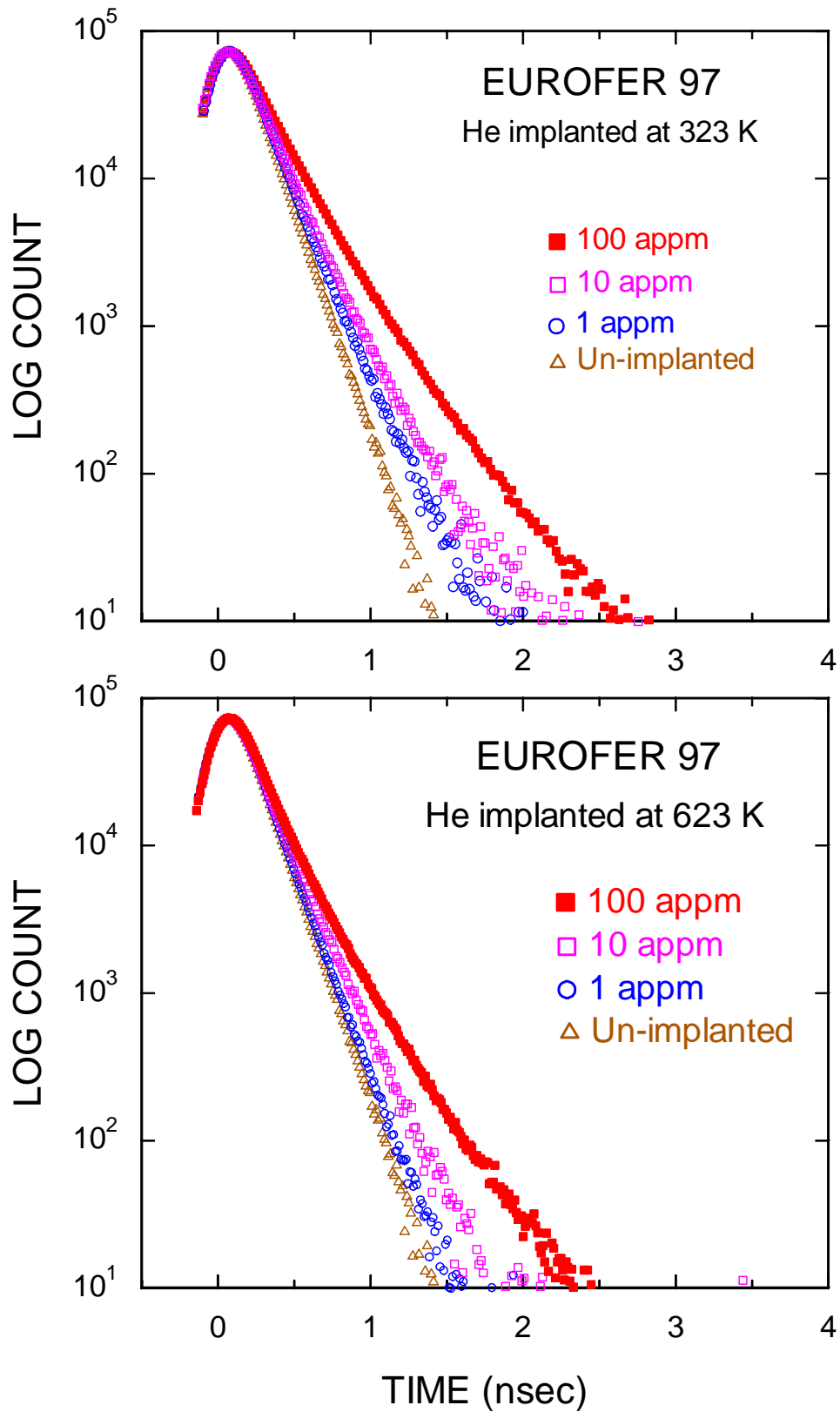
Figure 2. Positron lifetime spectra for Fe, which has been implanted with 1, 10, and 100 appm of helium at 323 K and 623 K. The increase of the average positron lifetime with increasing helium concentration reflects the formation of helium bubbles and other microstructural defects. The larger effect at 323 K than at 623 K reflect the formation of higher densities of very small cavities at 323 K. Note that implantation with 1, 10 and 100 appm He leads to displacement damage doses of 1.5×10^{-4}, 1.5×10^{-3} and 1.5×10^{-2} dpa, respectively (see Table 1).
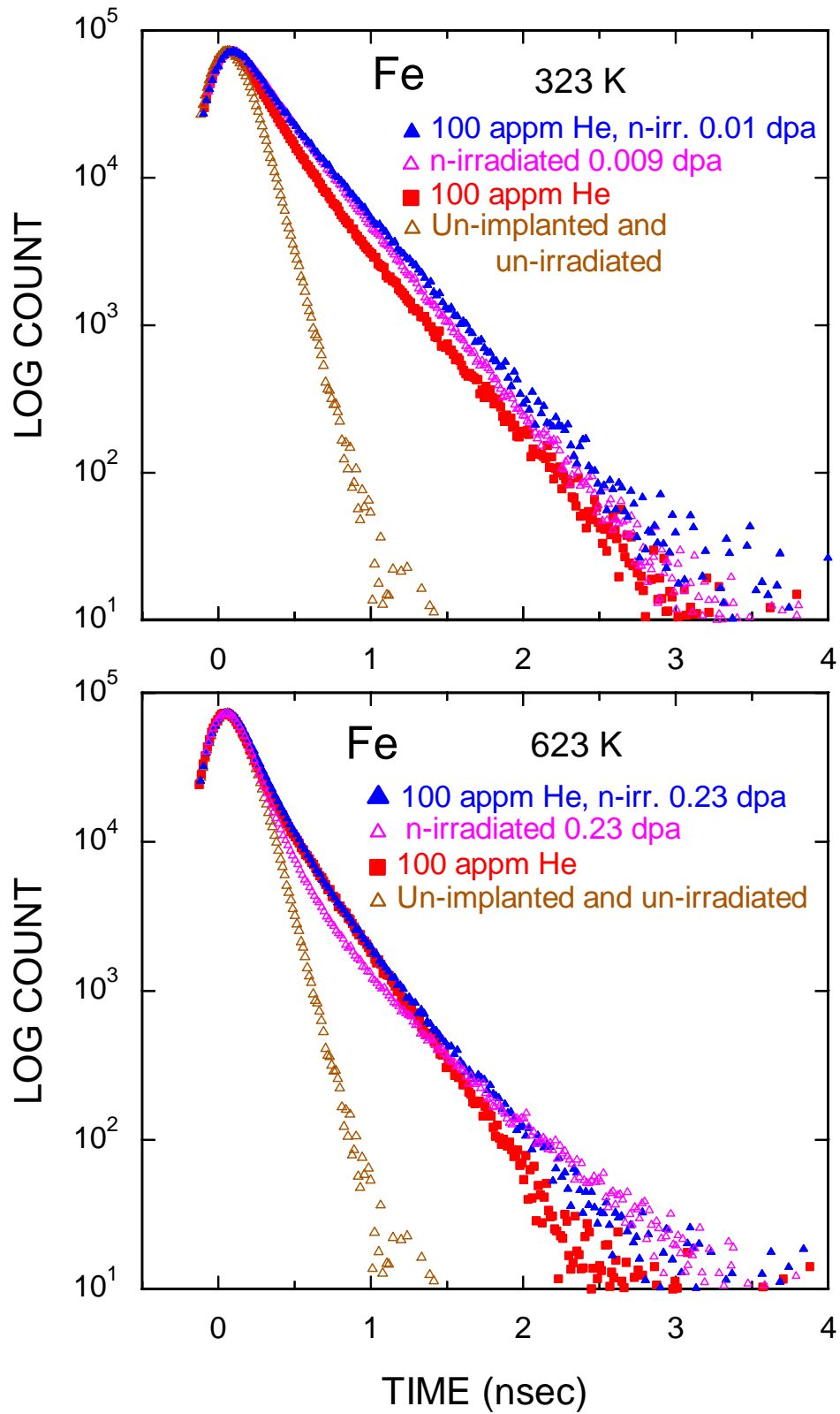
Figure 3. Comparison of positron lifetime spectra for iron, which has either been implanted with 100 appm helium, neutron irradiated or neutron irradiated after helium implantation. Both implantations and neutron irradiations were carried out at the same temperature, i.e. either at 323 K or at 623 K.
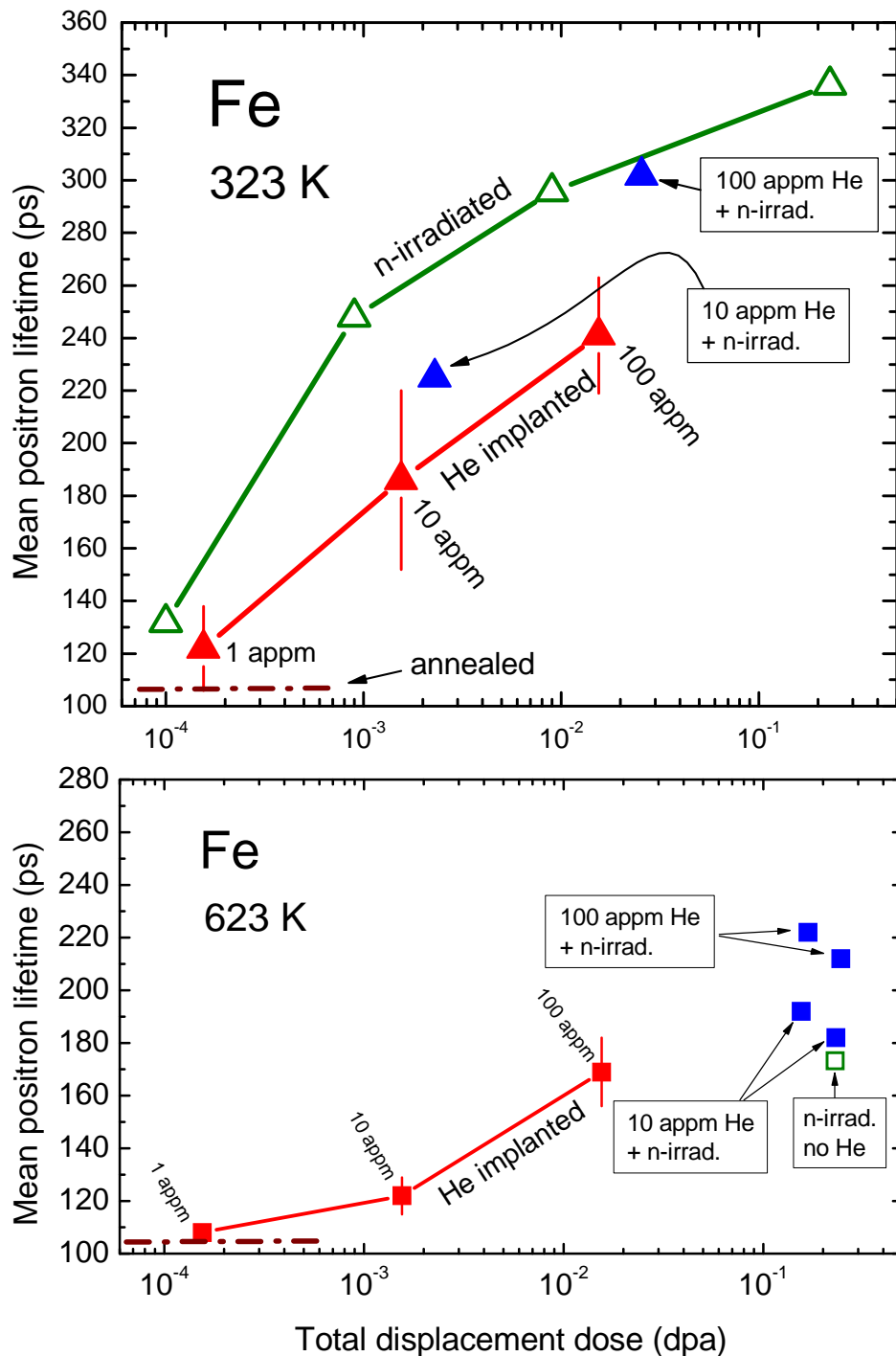
Figure 4. Mean positron lifetimes for iron which has either been implanted with helium, neutron irradiated or neutron irradiated after helium implantation. The points were calculated from spectra like the ones shown in Figs. 1 – 3. In the lower frame data are shown for samples which were Helium implanted, neutron irradiated or both at 623 K (implantation of 100 appm helium gives rise to a displacement dose of 0.015 dpa). For comparison, similar data are shown in the upper frame for implantation and/or irradiation temperatures of 323 K [7, 13]. The green open symbols are for neutron irradiation without helium implantation, while the blue filled symbols are results for neutron irradiation after implantation to a dose of 10 or 100 appm helium. An error bar associated with a red point indicates the scatter of results from several specimens implanted to the same nominal He dose.

Figure 5. Positron lifetime spectra for EUROFER 97 implanted with 100 appm of helium at 323 K and at 623 K. The larger effect of implantation at 323 K than at 623 K is due to the generation of a high density of small cavities at the lower temperature.

Figure 6. Positron lifetime spectra for EUROFER 97, which has been implanted with 1, 10, and 100 appm of helium at 323 K and 623 K. The effect of implantation is somewhat smaller than for iron (Fig. 1).
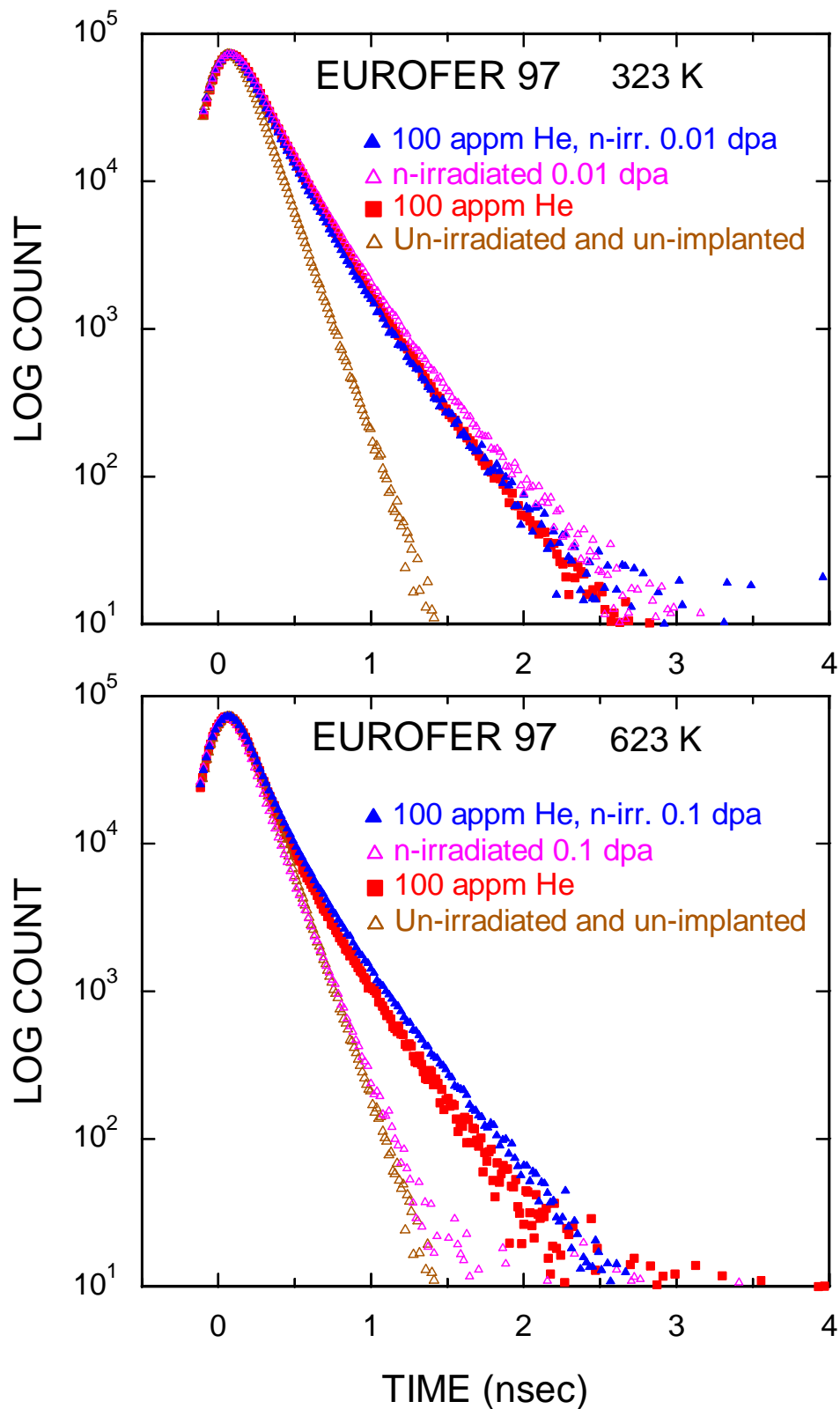
Figure 7. Comparison of positron lifetime spectra for EUROFER 97, which has either been implanted with 100 appm helium, neutron irradiated or neutron irradiated after helium implantation at 323 K or at 623 K. At 323 K the displacement dose seems to be the dominant factor (implantation of 100 appm helium gives rise to a displacement dose of 0.015 dpa), while the presence of He has only a minor effect. In contrast, at 623 K only a small effect of displacement damage is observed unless He is present.
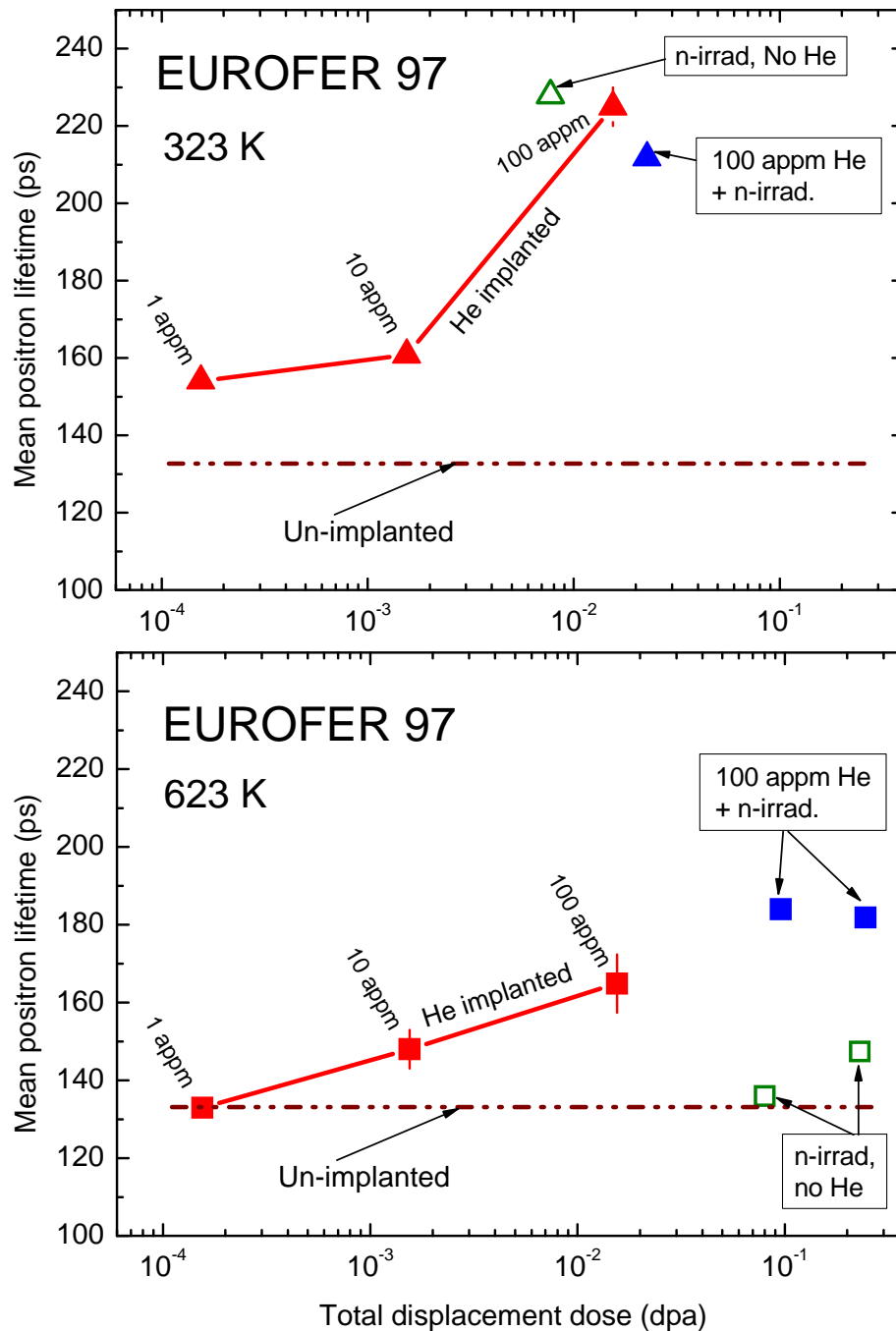
Figure 8. Mean positron lifetimes for EUROFER 97 which has either been implanted with helium, neutron irradiated or neutron irradiated after helium implantation. The points were calculated from spectra like the ones shown in Figs. 5 – 7. In the lower frame data are shown for samples which were Helium implanted, neutron irradiated or both at 623 K (implantation of 100 appm helium gives rise to a displacement dose of 0.015 dpa). For comparison, similar data are shown in the upper frame for implantation and/or irradiation temperatures of 323 K [13]. The green open symbols are for neutron irradiation without helium implantation, while the blue filled symbols are results for neutron irradiation after implantation to a dose of 100 appm helium. An error bar associated with a red point indicates the scatter of results from several specimens implanted to the same nominal He dose.
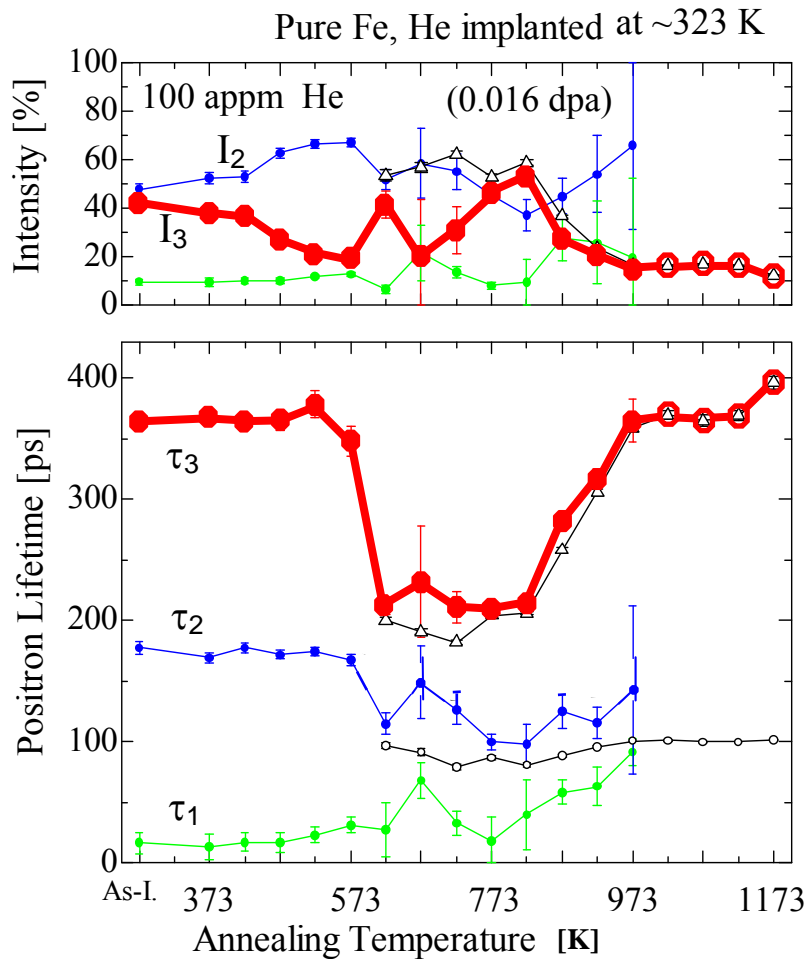
Figure 9. Positron lifetime parameters as functions of annealing temperature for pure iron implanted with 100 appm helium at ~323 K (no neutron irradiation). The longest lifetime τ_3 and its intensity I_3 (enhanced red curves) are due to He bubbles and/or nano-voids. A sharp annealing stage is observed at about 600 K. In the temperature range below 973 K three lifetime components have been resolved. The black points and curves for temperatures at and above 623 K indicate average lifetimes which were obtained if the measured lifetime spectra were approximated by only two lifetime components (collaboration with T. Toyama, Z. Tang, Y. Nagai and M. Hasegawa).
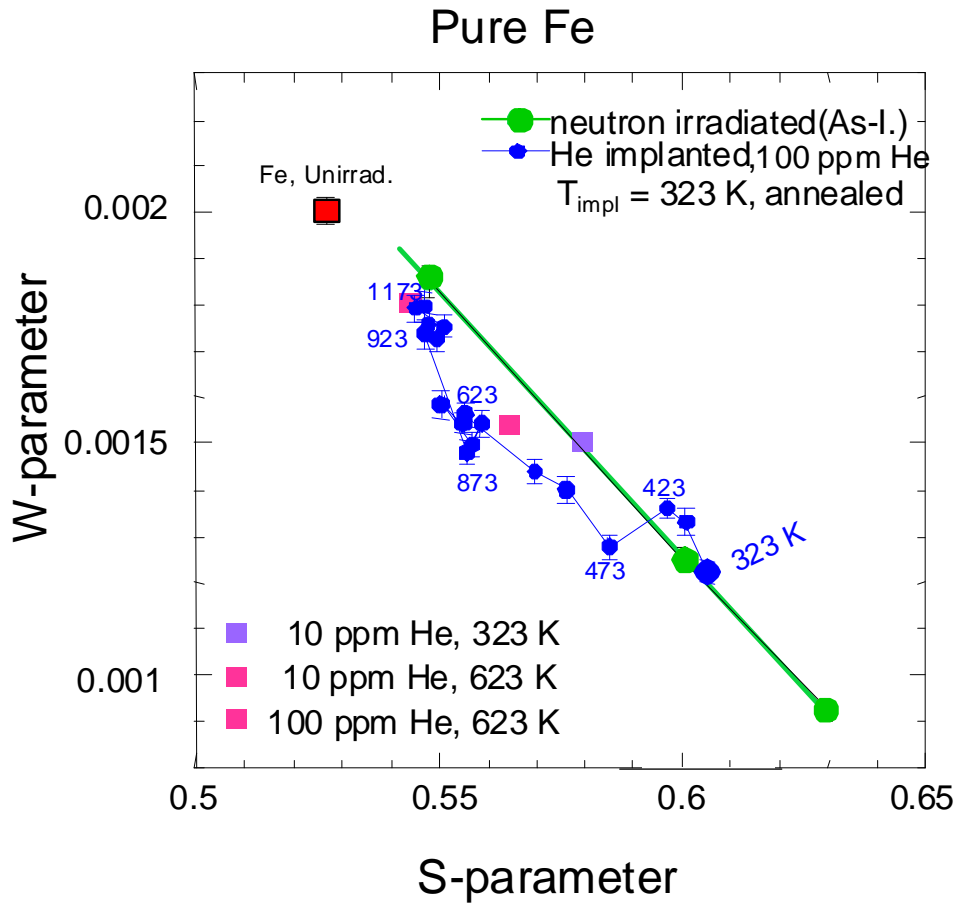
Figure 10. Correlation between S- and W-parameters derived from Coincidence Doppler Broadening measurements of iron specimens which were either 1) neutron irradiated to displacement doses of 10^{-4}, 10^{-3} and 10^{-2} dpa at ~ 323 K [7] (green points) or 2) implanted with 100 appm of helium at ~ 323 K and subsequently annealed (blue points with numbers indicating some of the annealing temperatures). The results for the different densities of nano-voids after neutron irradiation fall on a straight line, shown in green (see text). The deviation of the blue points from the green line is due to the effect of helium in the cavities. The CDB data were recorded simultaneously with the positron lifetime data shown in Fig. 9 (collaboration with T. Toyama, Z. Tang, Y. Nagai and M. Hasegawa).
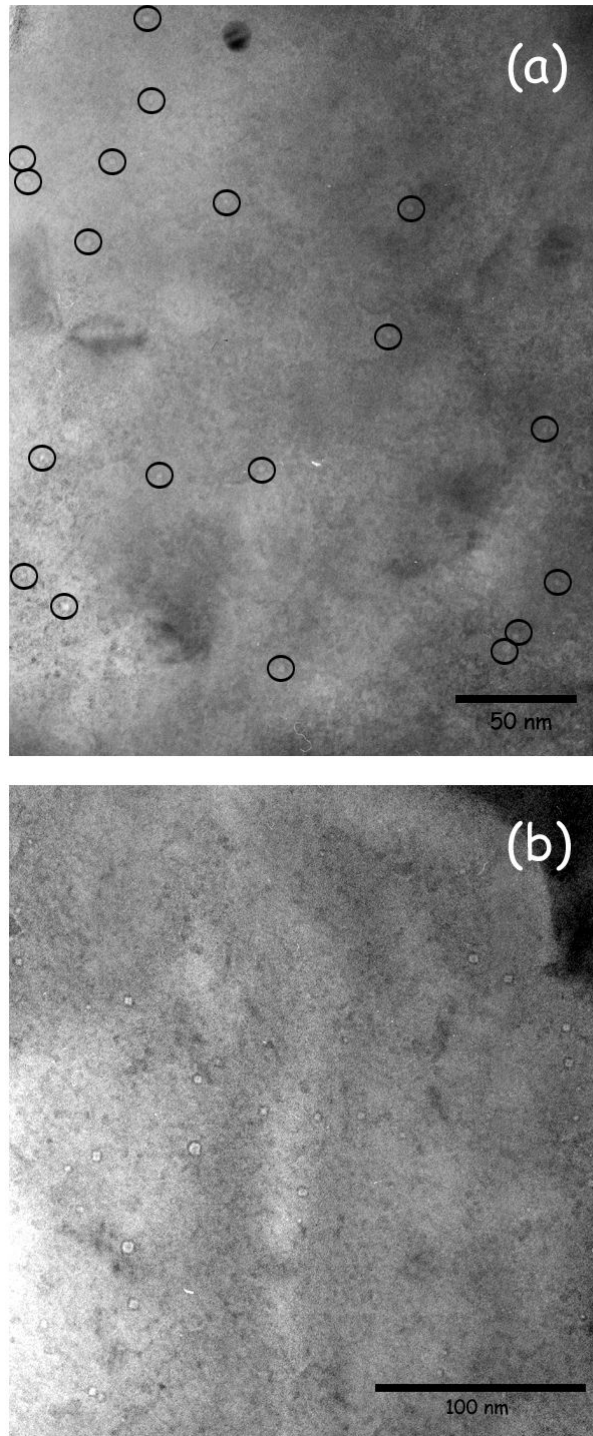
Figure 11. Transmission electron micrographs showing voids in pure Fe neutron irradiated at 623 K to a dose of (a) 0.08 dpa giving an average void size of ~ 2.5 nm and (b) 0.23 dpa giving an average void size of ~ 4.0 nm. In both cases the void density is about 1.5×10^{21} m^{-3}.
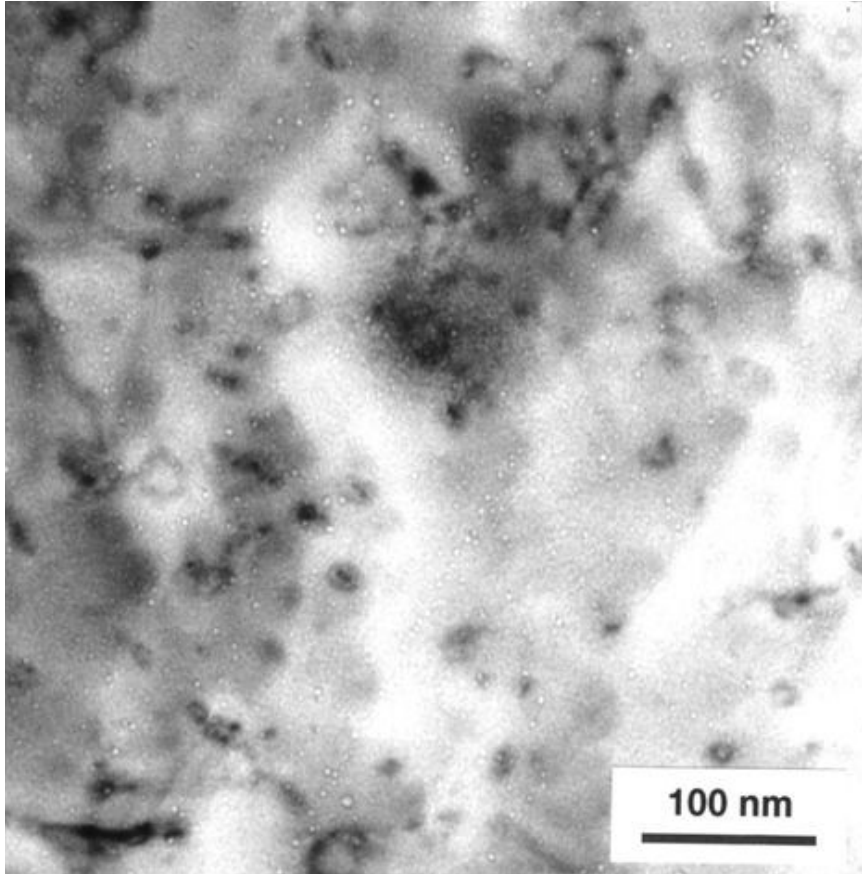
Figure 12. Transmission Electron Micrograph of Fe, implanted with 100 appm He and neutron irradiated to a dose of 0.23 dpa at 623 K. The observed cavities have an average size of ~ 3.5 nm and a density of ~ 1×10^{22} m^{-3}.
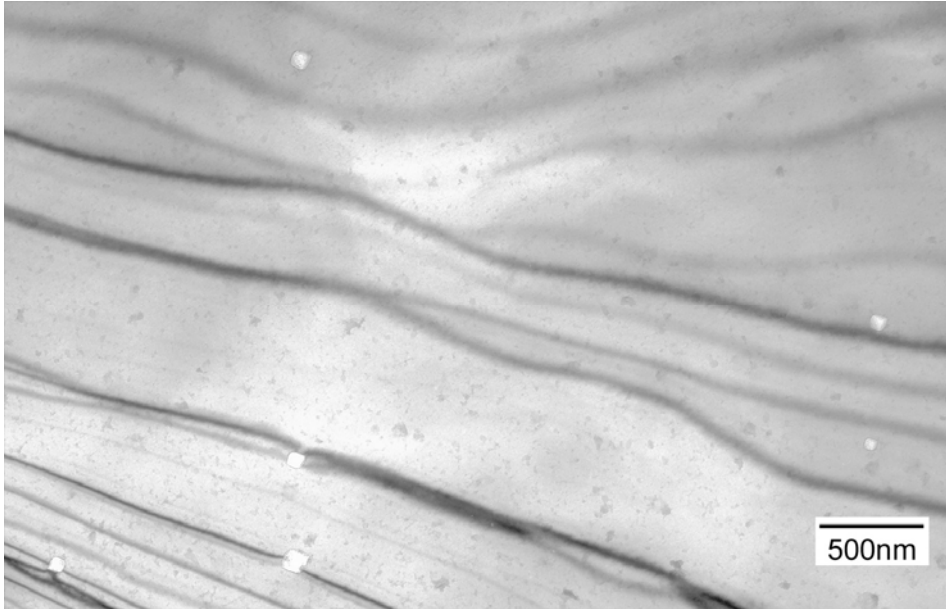
Fig. 13a. Transmission Electron Micrograph of pure iron neutron irradiated to a dose of 0.036 dpa at 323 K. Large voids (~90 nm) are observed with a relatively low density (~1×10^{19} m^{-3}) [24].
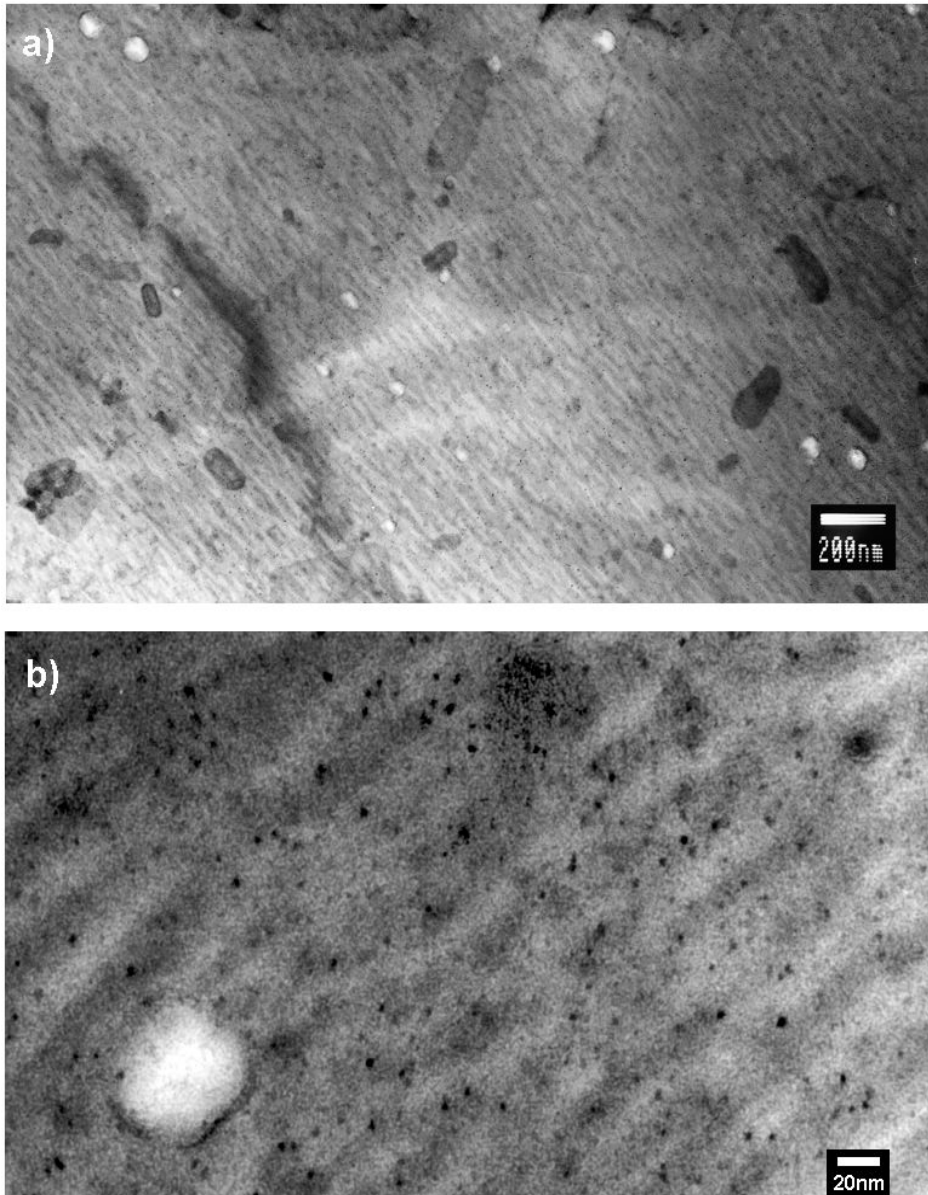
Fig. 13b. Transmission electron micrograph for pure iron implanted with 100 appm of helium at 323 K and subsequently neutron irradiated at 333 K to a dose level of 0.1 dpa showing: (a) relatively large voids (~52 nm in diameter) and (b) small (~4 nm in diameter) interstitial clusters. The density of voids and loops is estimated to be 2×10^{19} m^{-3} and 4×10^{22} m^{-3} [13].
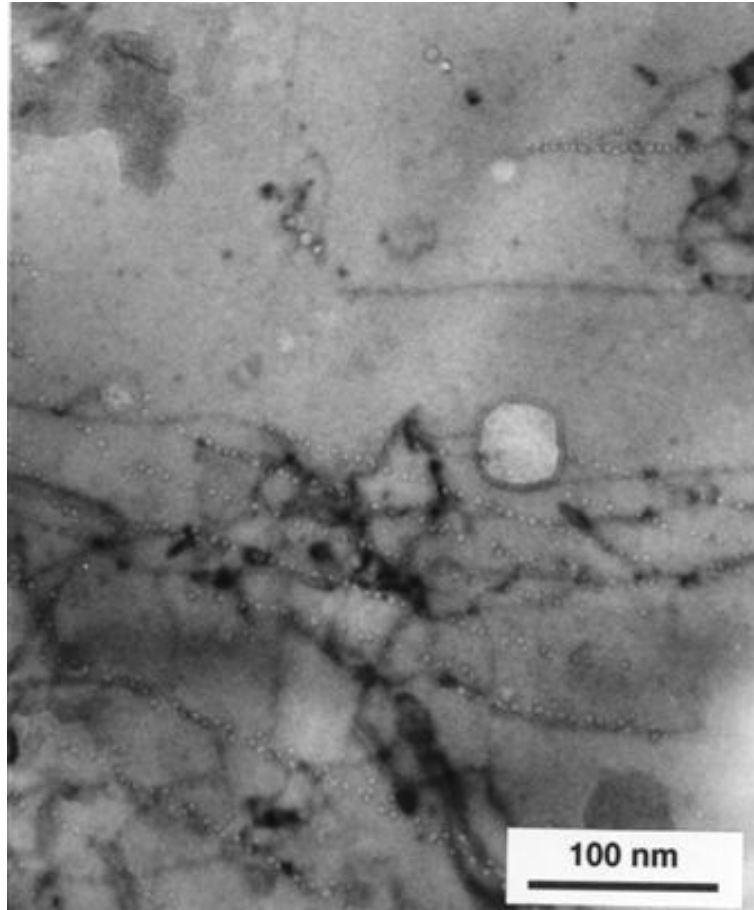
Figure 14. Transmission Electron Micrograph of EUROFER 97, implanted with 100 appm He and neutron irradiated to a dose of 0.23 dpa at 623 K. The observed cavities have a very inhomogeneous distribution. Cavities seem to form only at dislocations and interfaces, except for a very low density of large voids.
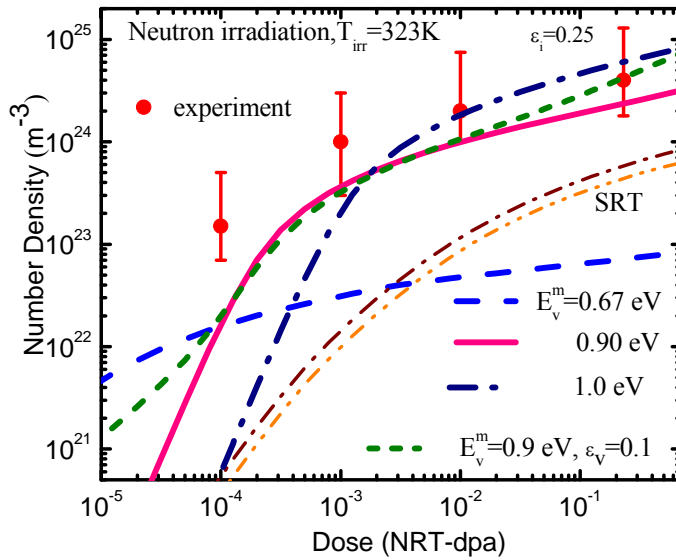
Figure 15. Calculated dose dependence of cavity density in neutron irradiated iron at 323K. Calculations have been done within the framework of PBM using different values of vacancy migration energy and cascade parameters (see text). For comparison the dose dependence of cavity density estimated by PAS [7] is also plotted. For comparison, the yellow and brown dash-dotted curves are calculated using Standard Rate Theory (SRT) with two different values of the dislocation bias (p = 0.04 and 0.4, respectively).
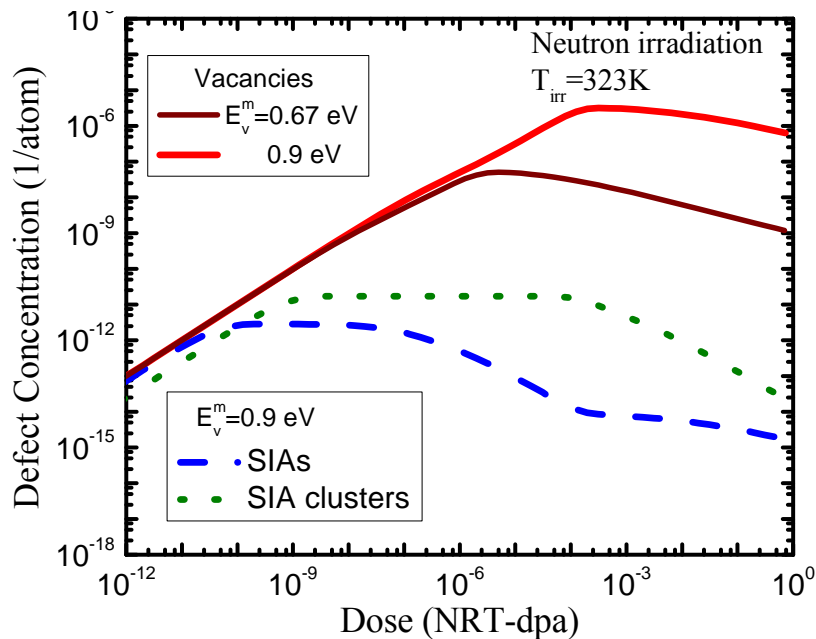
Figure 16. Dose dependence of the concentrations of mobile defects in neutron irradiated iron at 323K calculated for a vacancy migration energy equal to 0.9 eV. For comparison the vacancy concentration calculated with $E_v^m = 0.67$ eV is also presented.
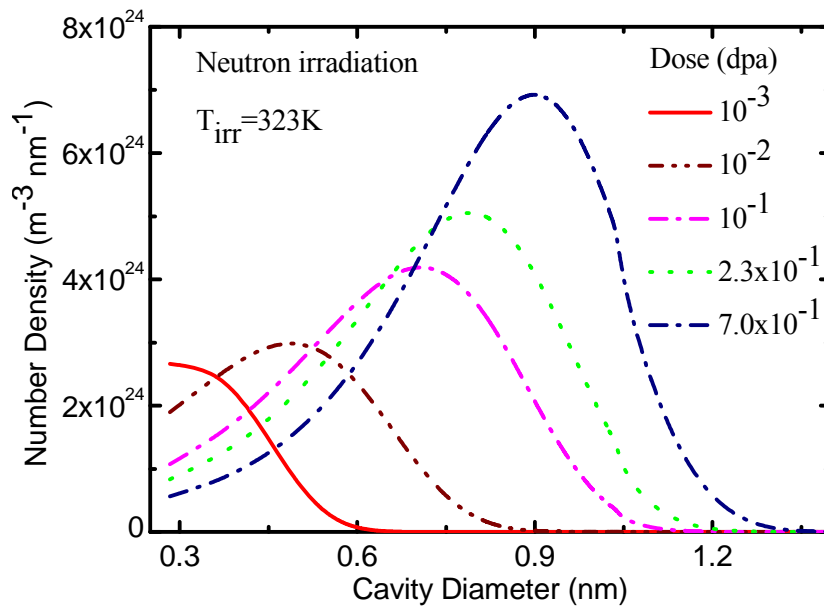
Figure 17. Calculated dose dependence of cavity size distribution function in neutron irradiated iron at 323K, using the same parameters as for the red curve in Fig. 15.
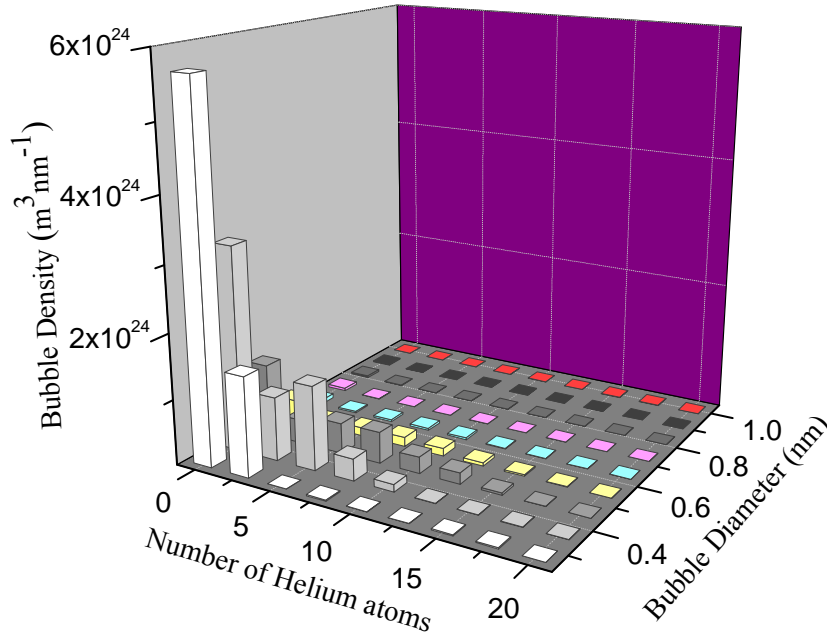
Figure 18. Calculated 2-dimensional cavity density distribution as a function of number of He atoms and cavity size for Fe after He implantation to a dose of 100 appm at a rate of 6×10^{-4} appm He/s at 323 K. A high density of cavities containing no or only a few He atoms dominates the size distribution.
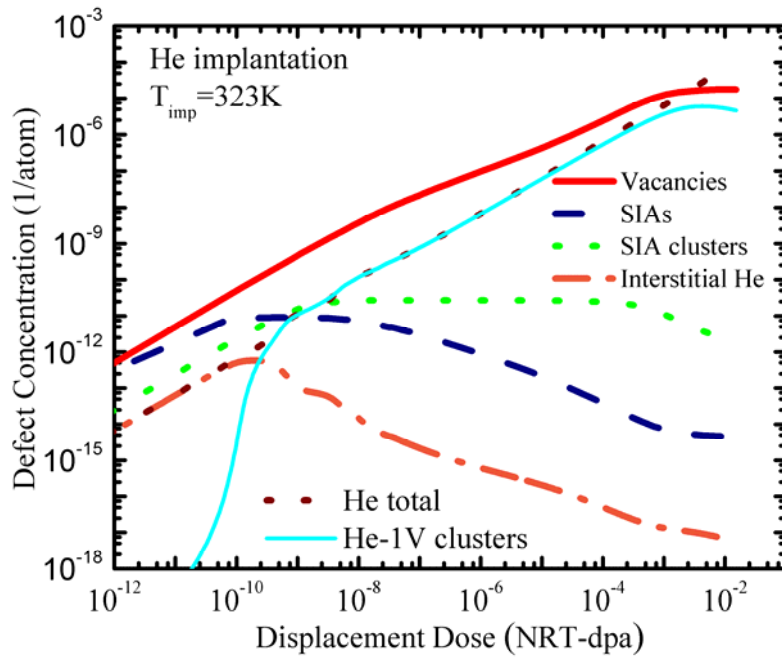
Figure 19. Calculated dose dependence of defect and defect cluster concentrations during He implantation at 323K.
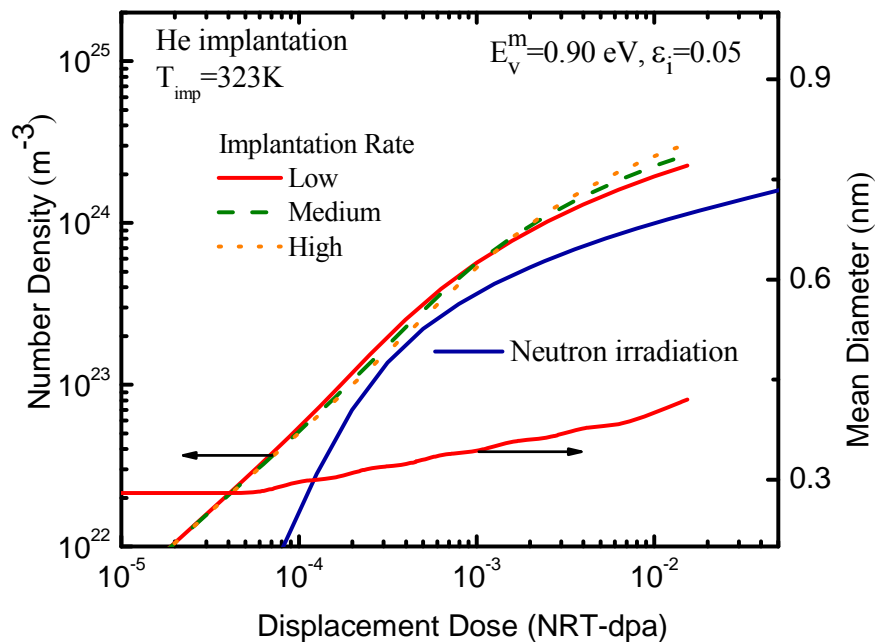
Figure 20. Calculated cavity density and size in iron as functions of displacement dose during helium implantation at 323 K for three different implantation rates: Low: 6×10^{-4} appm He/s, Medium: 1.8×10^{-3} appm He/s and High: 6×10^{-3} appm He/s (Table 6). For comparison, the calculated curve for neutron irradiated iron (from Fig. 15) is shown in blue.
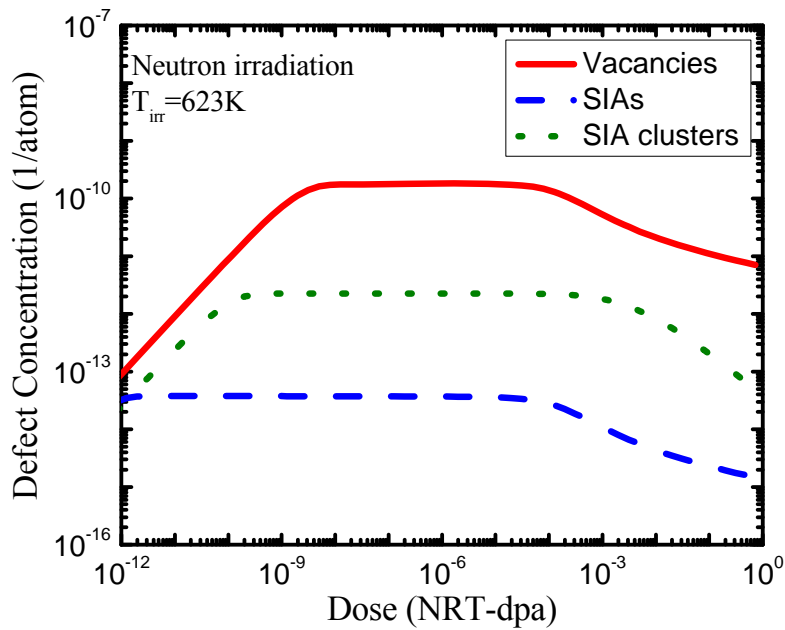
Figure 21. Calculated dose dependence of the concentrations of mobile defects in neutron irradiated iron without implanted He at 623K. Intra-cascade vacancy clustering was included in the calculations by taking $\varepsilon_v = 0.1$.
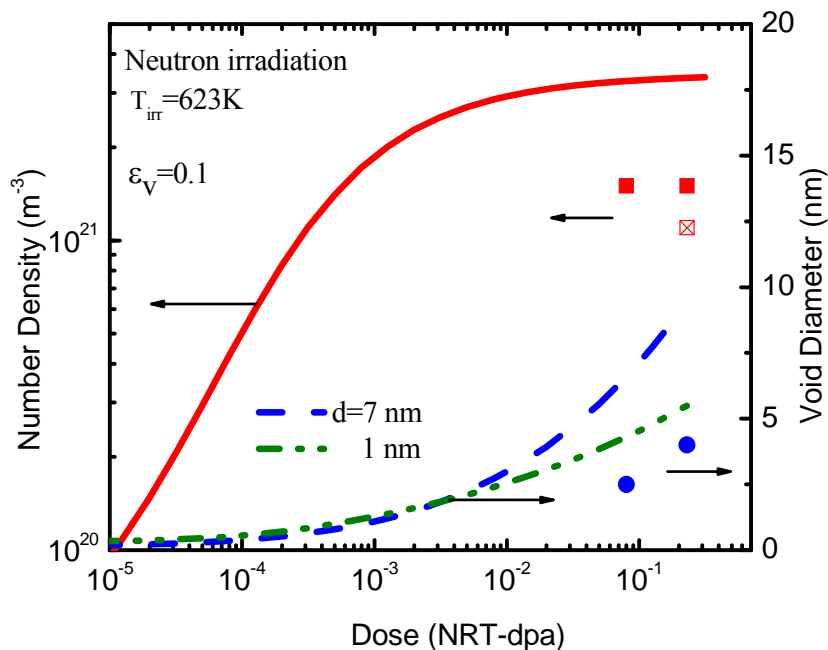
Figure 22. Dose dependence of density (red curve) and size (blue curve) of voids in neutron irradiated iron without implanted He at 623K. The blue circles and red squares shown for comparison are TEM results (Table 4). The red square with a cross is derived from PAS data (Table 3). The green dash-dotted curve was calculated within the framework of PBM assuming that the absorption diameter of dislocations for SIA clusters is only 1 nm. Note that the calculations have been done using cascade assisted void nucleation ($\varepsilon_v = 0.1$).
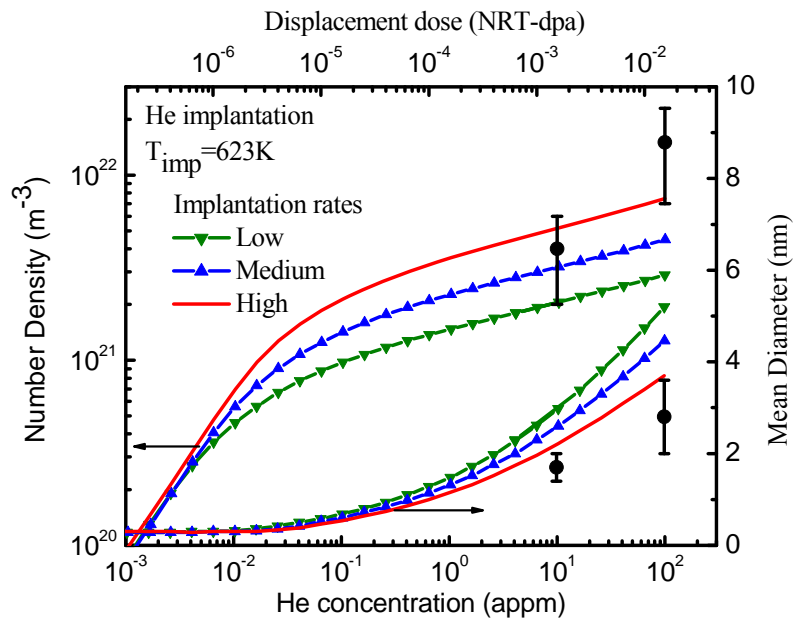
Figure 23. Calculated cavity density and size in iron as functions of He concentration (bottom scale) for helium implantation at 623 K. The upper scale shows the equivalent displacement dose. Calculations are shown for three different implantation rates: Low: 1.2×10^{-3} appm He/s, Medium: 3.6×10^{-3} appm He/s and High: 1.2×10^{-2} appm He/s (Table 6). For comparison, experimental values of densities and sizes of He bubbles in iron He implanted at 350ºC are shown by black dots. The latter were estimated by Positron Annihilation Spectroscopy (Table 3).
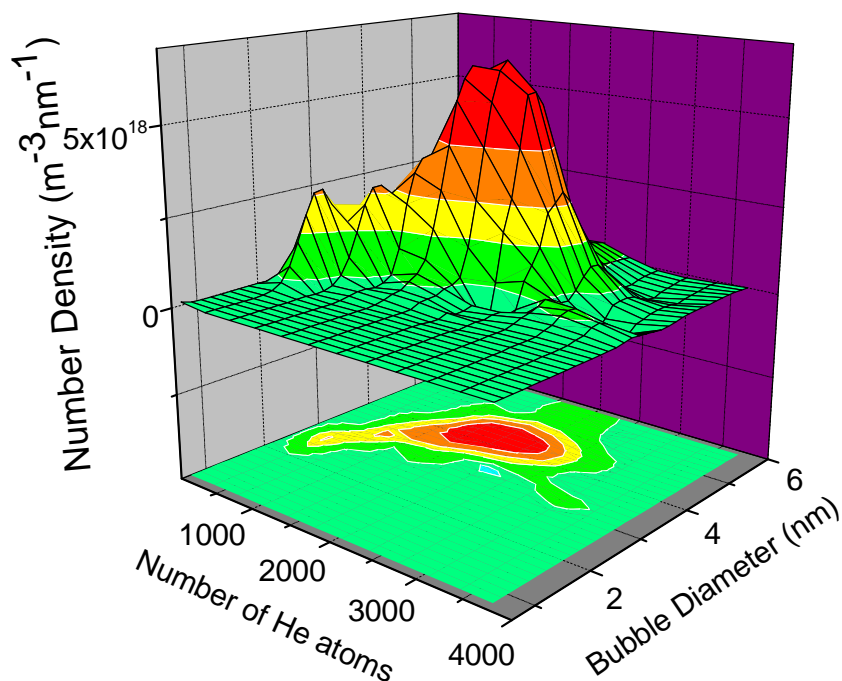
Figure 24. Calculated 2-dimensional cavity density distribution as a function of number of He atoms and cavity size for Fe after He implantation at 623 K to a He concentration of 100 appm with a rate of 1.2×10^{-2} appm He/s.
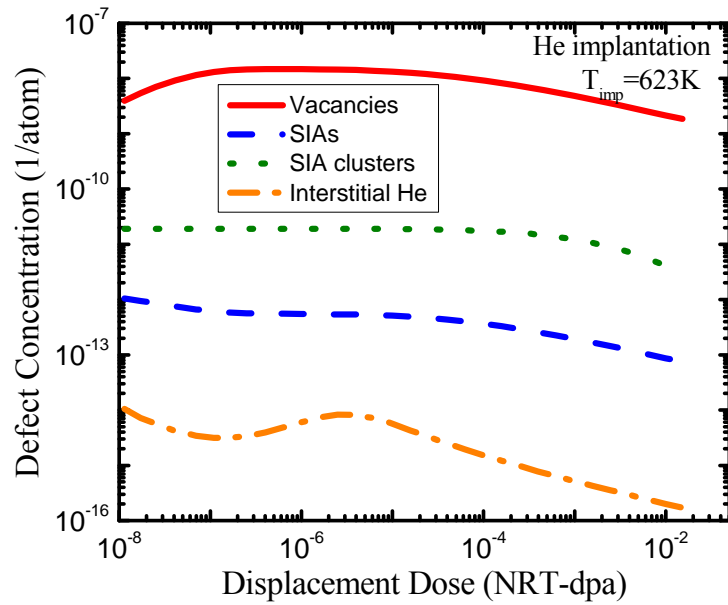
Figure 25. Calculated dose dependence of point defect concentrations in iron during He implantation at a rate of 1.2×10^{-2} appm He/s at 623K.
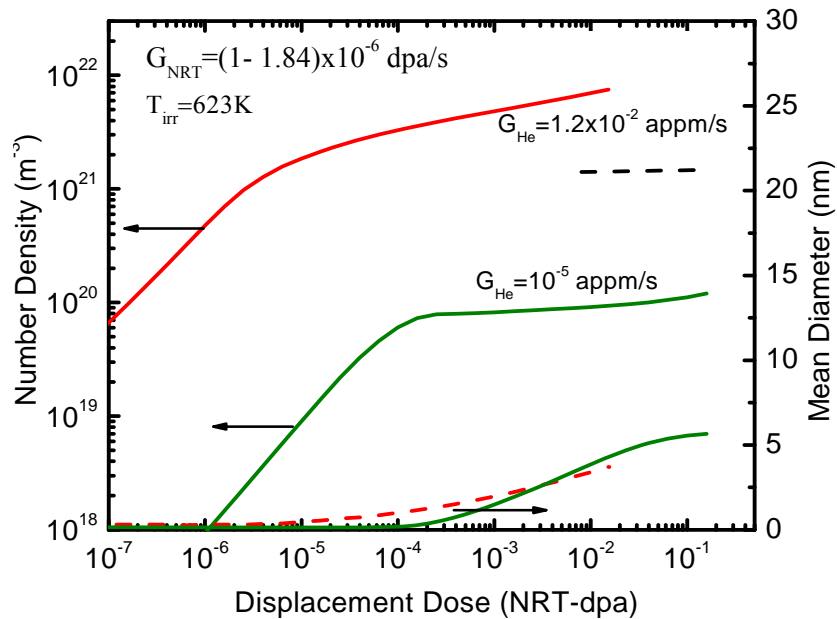
Figure 26. Effect of helium generation rate on cavity evolution at a given displacement rate and temperature. The calculations for cavity evolution with damage rate of $G_{NRT}=10^{-6}$ dpa/s and helium production rate of $G_{He}=10^{-5}$ appm/s (10 appm/dpa) are shown as green curves. The parameters correspond to damage conditions in the first wall of a fusion reactor made of an austenitic stainless steel. The fraction ε_i^g was taken to be equal to 0.25 (like for neutron irradiation). The red curves for 6500 appm/dpa are shown for comparison (from Fig. 23). The horizontal dashed black line indicates the experimentally determined cavity density after neutron irradiation (without implanted He) to dose values of 0.08 and 0.23 dpa (Table 4 and Fig. 22).
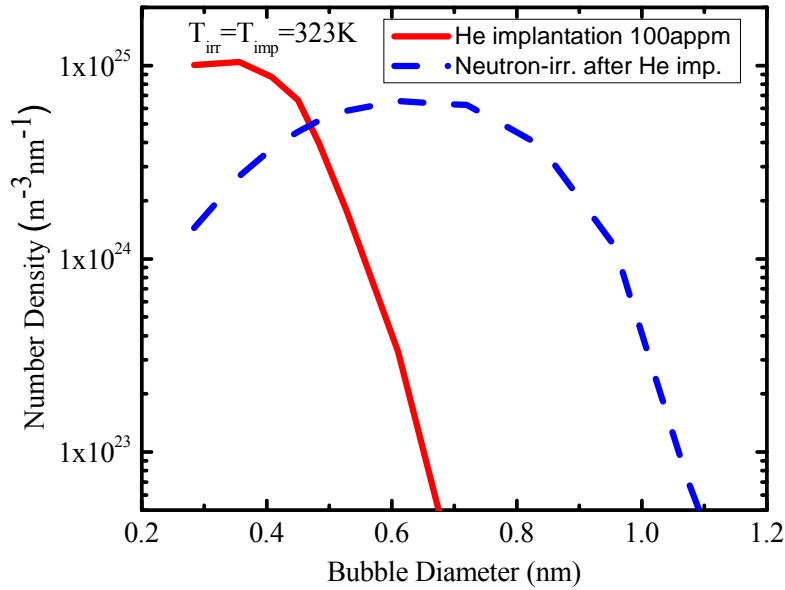
Fig. 27. Size distribution functions of cavities in iron calculated for the cases of 1) He implantation to a concentration of 100 appm He (red curve which is the one-dimensional SDF derived from Fig. 18 by integrating over all He contents for each cavity size) and 2) subsequently neutron irradiated to 0.23 dpa (blue dashed curve), both at 323K.
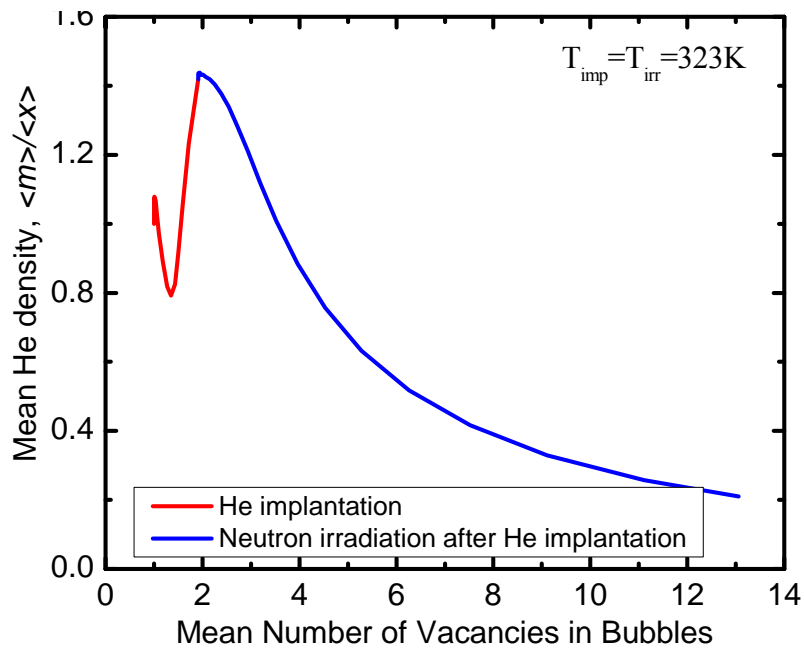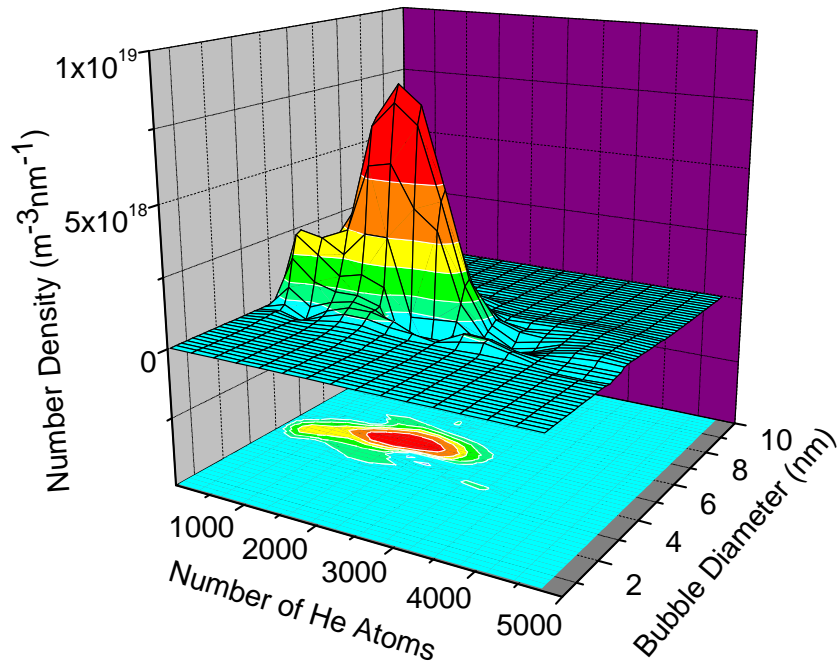

Fig. 28. Calculated evolution of the mean density of He in bubbles in iron during He implantation and followed by neutron irradiation, both at 323 K. The mean number of vacancies in bubbles increases with increasing displacement damage.

Fig. 29. Calculated 2-dimensional cavity density distribution in iron as a function of number of He atoms and cavity size after He implantation to a concentration of 100 appm He and subsequent neutron irradiation to a displacement dose of 0.023 dpa, both at 623 K.
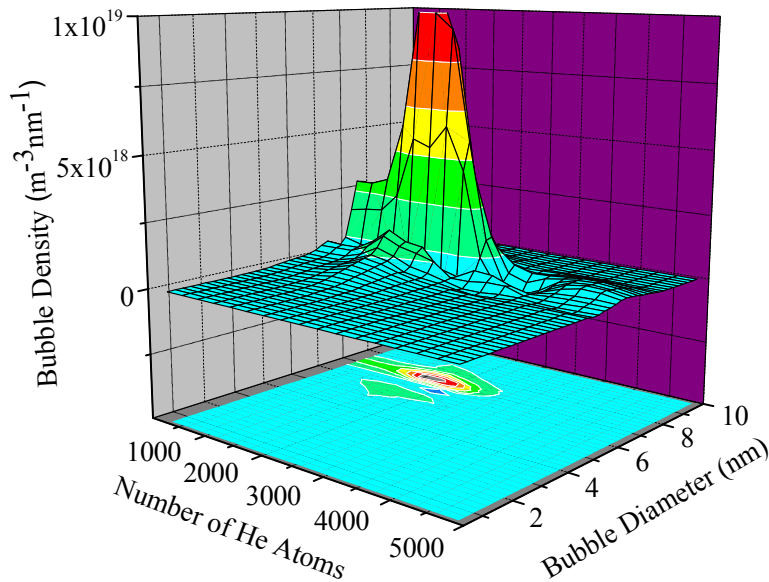

Fig. 30. Calculated 2-dimensional cavity density distribution in iron as a function of number of He atoms and cavity size after He implantation to a concentration of 100 appm He and subsequent neutron irradiation to a displacement dose of 0.23 dpa, both at 623 K.
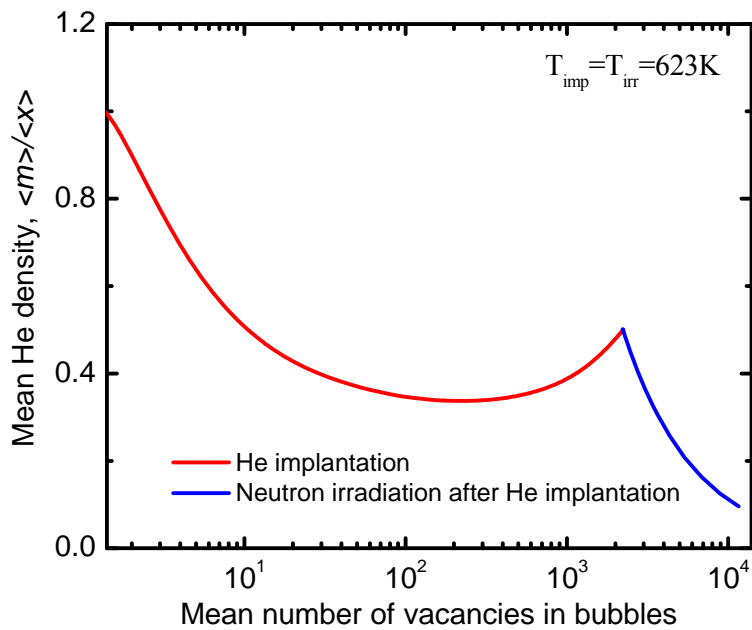
Fig. 31. Calculated evolution of the mean density of He in bubbles during He implantation up to a concentration of 100 appm He at 623 K followed by neutron irradiation at 623 K up to a dose of 0.23 dpa. Te mean number of vacancies in bubbles increases with increasing displacement damage.
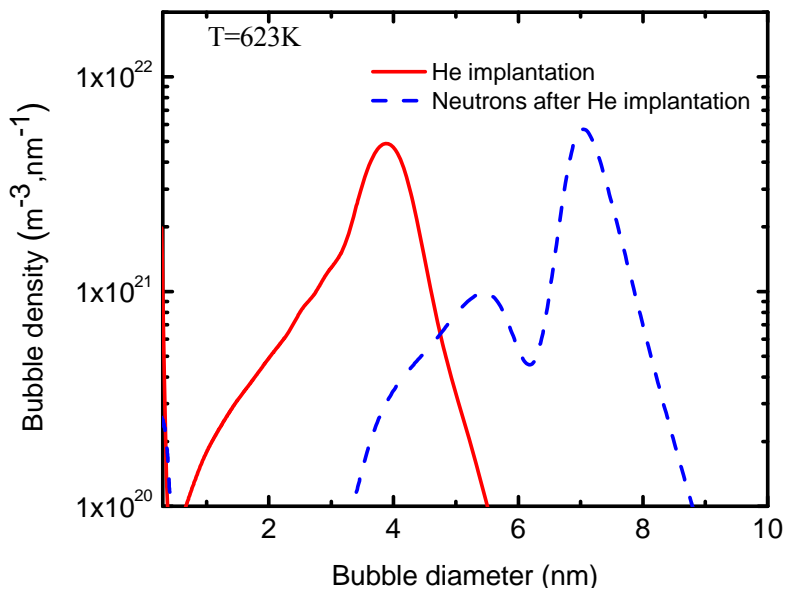

Fig. 32. Calculated size distributions of cavities in pure iron after helium implantation to a concentration level of 100 appm He at 623 K (red curve) as well as after neutron irradiation at 623 K to a displacement damage level of 0.23 dpa after the He implantation (blue curve).

Risø DTU is the National Laboratory for Sustainable Energy. Our research focuses on development of energy technologies and systems with minimal effect on climate, and contributes to innovation, education and policy. Risø has large experimental facilities and interdisciplinary research environments, and includes the national centre for nuclear technologies.